Evolution of Gas Velocity Dispersion in Discs from $z \sim 8$ to $z \sim 0.5$

E. Wisnioski[1,2,★] J. T. Mendel[1,2], R. Leaman[3], T. Tsukui[1,2], H. Übler[4,5,6], N. M. Förster Schreiber[6]
[1]Research School of Astronomy and Astrophysics, Australian National University, Canberra, ACT 2611, Australia
[2]ARC Centre of Excellence for All Sky Astrophysics in 3 Dimensions (ASTRO 3D)
[3]Department of Astrophysics, University of Vienna, Türkenschanzstrasse 17, 1180 Wien, Austria
[4]Kavli Institute for Cosmology, University of Cambridge, Madingley Road, Cambridge CB3 0HA, UK
[5]Cavendish Laboratory, University of Cambridge, 19 JJ Thomson Avenue, Cambridge CB3 0HA, UK
[6]Max-Planck-Institut für extraterrestrische Physik (MPE), Giessenbachstr. 1, D-85748 Garching, Germany

arXiv:2505.24129v1 [astro-ph.GA] 30 May 2025

Accepted XXX. Received YYY; in original form ZZZ

ABSTRACT

Together optical/near infrared integral field spectroscopy and resolved sub-millimetre interferometry data have mapped the ionised and molecular gas motions in nearly one thousand galaxies at redshifts $z > 0.5$. While these measurements have revealed a number of key properties about the evolution of disc structure and kinematics, heterogenous techniques and samples have led to disparate findings - especially when comparing different dynamical tracers (e.g., Hα, [C II], CO). In this paper we present a literature compilation of 237 disc galaxies with measurements of velocity dispersion and rotational velocity between $z = 0.5-8$, a subset of 63 galaxies have measurements of molecular gas fractions. We explore the connection between disc velocity dispersion measurements over 8 Gyrs as traced by multiple phases with the expectations from Toomre stability models. When sample properties are taken into account (e.g., stellar mass, tracer) there is little evolution in disc dispersions between $z \sim 1.5-8$, consistent with expectations from model assumptions. We find ionised gas dispersions are higher by $\sim 2\times$ from molecular gas dispersions at a fixed gas mass. These results are sensitive to the molecular gas tracer with results from [C II] showing mixed behaviour indicative of its multi-phase origin. The [C II] kinematics can be reconciled with molecular and ionised gas tracers when star-formation rates are taken into account.

Key words: galaxies: evolution – galaxies: high-redshift – galaxies: kinematics and dynamics

1 INTRODUCTION

Early *Hubble Space Telescope* (*HST*) results revealed a high fraction of galaxies with clumpy and irregular morphologies (e.g., Cowie et al. 1995; Glazebrook et al. 1995; van den Bergh et al. 1996). Since these early results, rich multi-wavelength datasets, including imaging, long slit, and integral field spectroscopy, have revealed that the majority of massive galaxies identified at cosmic noon, $z \sim 0.5-3$, are rotating discs (e.g., Elmegreen et al. 2007; Wuyts et al. 2011; Wisnioski et al. 2015). Many discs host transient regions of intense star formation that likely exist for no more than 200-500 Myrs (Guo et al. 2014; Wuyts et al. 2012). In addition to showing structures and rotation consistent with disc galaxies, both the morphological and kinematic data revealed 'puffy' discs (Reshetnikov et al. 2003; Elmegreen & Elmegreen 2006; Elmegreen et al. 2017) and high line of sight velocity dispersions (Förster Schreiber et al. 2006; Kassin et al. 2014; Wisnioski et al. 2015) suggestive of thick, turbulent, marginally stable discs. The large scale heights were interpreted as being consistent with gravitational collapse of kpc-sized clumps (Elmegreen & Elmegreen 2006; Bournaud et al. 2007; Wisnioski et al. 2012).

The *James Webb Space Telescope* (*JWST*) has largely confirmed these morphological results, although the higher resolution imaging of *JWST* reveals that discs were in place at even earlier times (Kuhn et al. 2024; Robertson et al. 2023; Lee et al. 2024b). Comparison with *HST* images reveal that galaxies at $z > 1$ are still on average clumpier than at $z = 0$ but that the increased resolution and longer wavelengths of *JWST* reveal more regular morphologies (Jacobs et al. 2023). The higher resolution allows for more disc features, such as bars, spirals, and lopsidedness, to be explored, revealing a complexity of disc galaxy morphology both in young and old stars (Le Bail et al. 2023). Galaxies are confirmed to already host thick stellar discs at $z \sim 4$, when exploring the rest-frame optical/IR light, with typical scale heights of $\sim 0.4-0.5$ kpc, albeit with large scatter (Lian & Luo 2024; Tsukui et al. 2024).

Since the first hints of early kinematic discs from ALMA data (Smit et al. 2018), there has been a steady growth of results at $z > 4$ for cool gas discs (e.g., Tadaki et al. 2018; Jones et al. 2021; Tsukui & Iguchi 2021; Fujimoto et al. 2021; Herrera-Camus et al. 2022; Posses et al. 2023) extended now by *JWST* to also include ionised gas discs (Nelson et al. 2023b; Vega-Ferrero et al. 2023; Huertas-Company et al. 2023; Bacchini et al. 2024). Surprisingly, a number of the observations have revealed, not just a high fraction of galaxies dominated by rotation, but massive early discs (Nelson et al. 2023b) and dynamically 'cold' discs with molecular gas dispersions as low as ~ 15 km/s (Rizzo et al. 2020, 2021; Fraternali et al. 2021) – seemingly in contention with the ionised gas results at 'cosmic noon'. Simulations suggest that the presence of early cold discs could result from co-planer gas accretion (Kretschmer et al. 2022), which has been shown to correlate with disc stability (Jiménez et al. 2023). Other

★ E-mail: emily.wisnioski@anu.edu.au

© 2025 The Authors

simulations suggest that the observational results are consistent with the formation of a thin molecular gas disc where a thicker ionised gas disc forms due to stellar winds and other energy injecta (Meng et al. 2019; Rizzo et al. 2022; Kohandel et al. 2024). Indeed, the multi-phase nature of discs is often ignored in observations due to difficulty in obtaining resolved measurements in different wavebands or across different facilities due to $\sim$ 20 hour on source integration times. However, some studies compiling samples from the literature have shown a consistent offset between the kinematics of ionised and molecular gas discs (Übler et al. 2019; Girard et al. 2021; Rizzo et al. 2024).

The evolution of disc galaxies has far-reaching implications with respect to galaxy structure, chemical distribution, and star formation processes. Quantifying the zero-age velocity dispersion, or birth dispersion, of stars can reveal the relative importance of other heating mechanisms over cosmic time (e.g., Leaman et al. 2017; McCluskey et al. 2024; Hamilton-Campos et al. 2023). In the context of the Milky Way, many theories and simulations support a 'born-hot scenario' in which the early interstellar medium (ISM) of the Milky Way is already turbulent and settles over time as subsequent stellar populations are born (Belokurov & Kravtsov 2022). More generally, this can be considered as 'upside-down' growth (Bird et al. 2013, 2021). However, other simulations reveal galaxies that form initially as dynamically cold molecular discs in their centers (Tamfal et al. 2022). Even if stars are born dynamically 'warm,' additional heating is expected to occur through well known internal processes, including GMC scattering (Spitzer & Schwarzschild 1951) and radial migration (Sharma et al. 2021). Mergers, e.g., Gaia-Enceladeas in the Milky Way, provide an external heating mechanism that is commonly implemented in simulations (e.g., Font et al. 2001). However, small variations in mass ratios and growth histories of mergers can have a large effect on final galaxy structures (Rey et al. 2023). Constraining the relative amount and time of heating mechanisms together with star formation histories has the potential to explain the commonality of structures across cosmic time (e.g., thin-thick disc dichotomy; Mackereth et al. 2019; Leaman et al. *in prep*).

Combining the high-redshift studies with other approaches to the cosmic evolution of discs is complicated by observations with limited spatial and spectral resolution. Observations at high redshift are subject to poor spatial resolution relative to the observational beam size or point spread function (PSF). The result, typically referred to as beam smearing, elevates the line of sight velocity dispersion (Davies et al. 2011). The effect is most severe where the velocity gradient, $\Delta V/\Delta R$, is greatest. This occurs at the centre of the galaxy where the star formation peaks, but is dependent on other factors such as inclination, galaxy size relative to beam size, the shape of the PSF, central mass concentration (bulge), etc. (Burkert et al. 2016). Forward modelling codes have been developed to account for the beam when fitting disc models (e.g., Bouché et al. 2015; Di Teodoro & Fraternali 2015) however these codes must assume a disc model and often work only on the highest signal to noise data and most regular/symmetric rotators (Di Teodoro et al. 2016; Lee et al. 2024a). Forward modelling three dimensional data cannot fundamentally recover intrinsic velocity structures that are poorly resolved due to degeneracies among flux, rotation, and velocity dispersion distribution.

Limits on spectral resolution for optical and near-infrared instruments result in large uncertainties, especially if intrinsic dispersions are below $\sim$ 30 km s^{-1} (Wisnioski et al. *in prep*). These uncertainties contribute to the larger scatter when looking at population statistics, making it difficult to uncover correlations with key properties (e.g., star formation rates; Übler et al. 2019). New instruments are now available (ERIS; Davies et al. 2018) and are being developed (MAVIS; Ellis et al. 2020) with higher spectral resolutions to provide better constraints on dispersions below the resolution limits of past facilities.

In this paper, we aim to unite the mainly optical/near-infrared dispersion results at 'cosmic noon' ($0.5 < z < 3$) with the molecular gas and new *JWST* results out to 'cosmic morning' ($3 < z < 8$; Section 2). We compare the data compilation spanning 12 Gyrs with the analytic model in Wisnioski et al. (2015) and provide an updated model using recent literature results (Section 3). We discuss the role of gas phase tracer in mapping the evolution of dispersion in Section 4. We assume a Chabrier (2003) initial mass function and and assume a flat ΛCDM cosmology with $\Omega_{\rm m} = 0.3$ and $H_0 = 70$ km s^{-1}Mpc^{-1}.

2 LITERATURE COMPILATION

In this section we present a heterogeneous data compilation of galaxies observed primarily from $z \sim 0.5 - 8$, corresponding to lookback times of 5 – 12.8 Gyrs. We focus on this redshift range due to the apparent tension between recent results. Local galaxies are not included in the compilation. They have been explored in detail in this context (e.g., Green et al. 2010; White et al. 2017; Johnson et al. 2018; Varidel et al. 2020; Girard et al. 2021; Law et al. 2022). For this work, we include galaxies with dispersions measured from resolved spectral features arising from optical emission lines (Hα, [O III]) and far-infrared (FIR) / sub-millimetre emission lines ([C II], [O I] , CO transitions). We include measurements that have been made with a variety of instruments and derived with different techniques. We also include lensed and non-lensed galaxies. A brief discussion on the impact of heterogeneous aspect of the data compilation is given in Section 2.3. It is worth noting that the datasets for the different gas phases have little overlap and there has yet to be a significant sample of galaxies resolved kinematically with both an ionised and molecular gas tracer beyond $z \sim 0$. In some cases, resolved ionised gas kinematics are available for the same sources as unresolved cold gas measurements (providing gas mass estimates; as discussed in Section 2.2). Table 1 gives the literature sources used.

Literature data have been adjusted to a Chabrier IMF for stellar masses. The sample is also heterogeneous in the derivation of these parameters with a different level of constraints due to the availability of photometric bands for spectral energy distribution (SED) fitting. For consistency, we exclude a handful of sources where stellar masses are derived using scaling relations between UV luminosity and stellar mass (e.g., Shao et al. 2022; Parlanti et al. 2023). Star formation rates (SFRs) are derived from a number of techniques including optical emission lines, SEDs, and [C II] emission. The variety of measurements, which trace star formation of different timescales, may lead to increased scatter (e.g., Boselli et al. 2002; Schaerer et al. 2020).

We focus on galaxies that have been classified as discs. This focus is for fair comparison in Section 3 to theoretical models of disc galaxies. We note, however, that this adds bias to the sample. To classify something as a disc is difficult and depends on the adopted definition of 'disc' (Rodrigues et al. 2017; Simons et al. 2019). Differentiating between isolated discs and discs currently undergoing a merger, or resulting from a recent gas-rich interaction, requires either deep imaging and/or high-density spectroscopic surveys currently beyond reach. Distinguishing between a disc and a close pair that is beam-smeared to appear as a disc is typically possible in deep high-quality multi-wavelength data using stellar and gas morphology and information from velocity fields (Shapiro et al. 2008;

Table 1. Included datasets for this data compilation, N denotes the number of sources, z gives the redshift or redshift range and the last column notes if sources are gravitationally lensed. Some sources have multiple references listed where galaxy properties are taken from multiple sources. Some sources have measurements from multiple lines and are counted twice to reach N=245 total measurments.

Paper	N	z	Lensed?	Lines	Measurement Technique[a]
optical line tracers					
Tacconi et al. (2013)	1	1.5	n	Hα	data
Übler et al. (2019)	175	0.6-2.7	n	Hα	DysmalPy
Übler et al. (2024a)	1	4.1	n	Hα	DysmalPy
Fujimoto et al. (2024)	1	6.1	y	Hα, [O III]	3D-BAROLO
FIR/sub-mm line tracers					
Tacconi et al. (2013)	6	1.1-1.5	n	CO(3-2)	data
Übler et al. (2018)	1	1.4	n	CO(3-2)	DysmalPy
Swinbank et al. (2011)	1	2.3	y	CO(1-0)	data
Tadaki et al. (2020a),	1	4.3	n	[C II]	GalPak
Neeleman et al. (2020b)	1	4.3	n	[C II]	QubeFit
Rizzo et al. (2020)	1	4.2	y	[C II]	Rizzo+18
Lelli et al. (2021)	1	4.8	n	[C II]	3D-BAROLO
Tsukui & Iguchi (2021)	1	4.4	n	[C II]	data
Fraternali et al. (2021)	1	4.6	n	[C II]	3D-BAROLO
Rizzo et al. (2021)	5	4.2-4.7	y	[C II]	Rizzo+18
Jones et al. (2021)	6	4.4-5.5	n	[C II]	3D-BAROLO
Posses et al. (2023)	1	6.8	n	[C II]	3D-BAROLO
Rizzo et al. (2023)	18	0.5-3.6	n	CO(2-1), CO(3-2), CO(5-4), CO(6-5), [C I]	3D-BAROLO
Parlanti et al. (2023)	8	5.2-7.7	n	[C II] , [O III]	KinMS
Fujimoto et al. (2024)	1	6.1	y	[C II]	3D-BAROLO

[a] Technique used to measure kinematic parameters: data = data driven techniques including using the outer regions; DysmalPy (Price et al. 2021); GalPak3D (Bouché et al. 2015); KinMS (Davis et al. 2013); QubeFit (Neeleman et al. 2020a); Rizzo+18 (Rizzo et al. 2018); 3D-BAROLO (Di Teodoro & Fraternali 2015).

Wisnioski et al. 2015). However, many sources, especially at $z \gtrsim 3$, don't have deep multi-wavelength data required to be unequivocally classified. It is possible for sources previously identified as discs, or 'candidate discs', with kinematics resolved by multiple beams (e.g., Herrera-Camus et al. 2022) to be reclassified as mergers (Parlanti et al. 2024) with higher resolution data or information from different wavelengths. For the purposes of this paper and comparison to theoretical models we make a broad definition of 'disc' galaxy to include galaxies supported by rotation simply by the measurement of $V/\sigma > 1$ or as identified in the original papers. We acknowledge that this likely includes non-virialised discs and discs in the process of merging.

2.1 Ionised gas with rest-frame optical observations

Data compilations have been made at cosmic noon by a variety of authors which show good agreement amongst samples (Wisnioski et al. 2015; Übler et al. 2019). For this work, we include resolved ionised gas observations at cosmic noon primarily from the KMOS^{3D} survey using Hα. At higher redshifts, we include new JWST results (e.g., Übler et al. 2024b). Although some of these results are not taken with IFUs they are among the first measurements of kinematics of ionised gas discs at $z > 4$ available and thus included for an initial comparison with $z > 4$ cold gas discs. While the focus of this paper is on kinematics derived from 3D data, we note that agreement is usually seen between high-quality long-slit and IFU data (e.g., Kassin et al. 2014; Price et al. 2016) with some deviations (Übler et al. 2024a). Details for the various compiled samples are given in Table 1. Some kinematics, particularly the samples at $z \sim 3$ and $z \sim 7$ have been derived using forbidden lines, e.g., [O III] λ4959, 5007. There has been some work showing that the kinematics of gas traced by the forbidden lines can differ than gas traced by the Balmer lines (Law et al. 2022; Übler et al. 2024a).

2.2 Multi-phase gas with millimeter observations

As with ionised gas, the kinematics of cooler gas has been traced by different emission lines including CO transitions, [C I] transitions, and [C II] 158μm. However, these lines are not a direct tracer of the molecular gas and have been shown to trace in some cases a mixture of densities, temperatures, and phases (e.g., Zanella et al. 2018; Clark et al. 2019; Madden et al. 2020; Dunne et al. 2022). We include the PHIBSS (Tacconi et al. 2013) and ALPAKA (Rizzo et al. 2023) surveys and many papers with one or a handful of galaxies. The millimeter compilation, primarily coming from the higher redshift universe, $z > 3$, is more heterogeneous than the ionised gas compilations as it is difficult to observe large samples due to long integration times. There have also been comparably fewer deep multi-wavelength photometric and spectroscopic surveys to select mass-complete or representative samples.

The molecular gas masses and stellar masses are also collected for the millimeter data compilation. We have re-derived molecular gas masses where possible using the provided line or dust luminosities to homogenise assumptions and accepted conventions for converting luminosities to molecular gas masses. This allows for consistent assumptions (e.g., α_{CO}, handling higher J transitions) across datasets.

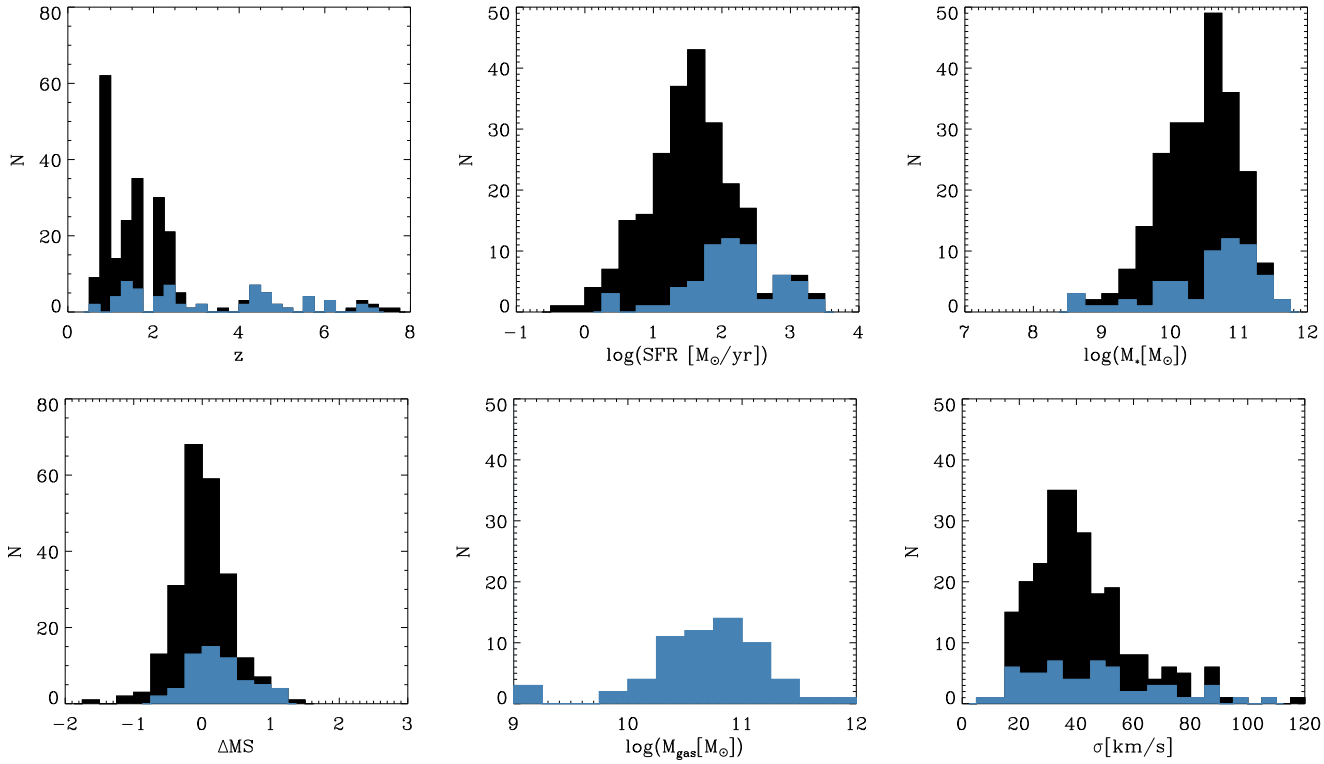

Figure 1. Summary of properties of literature compilation. Black histograms indicate the full sample, the blue histograms indicate the sub-sample that have measured molecular gas masses as shown in the middle panel of the bottom row.

For galaxies with measurements of resolved [CII] and unresolved CO we utilise the [CII] measurements for the kinematics but preference any unresolved CO measurements for estimates of molecular gas masses.

For galaxies with available CO measurements, we started with flux measurements reported in the literature. Converting from high-J CO flux to CO(1-0) flux, we adopt Table 2 of Carilli & Walter (2013) for quasars (QSOs) and sub-milimetre galaxies (SMGs; as identified in the original papers). The compilation includes 16 SMGs and 2 QSOs. For normal main sequence (MS) galaxies, we used $R_{21} = 0.9$ (Carilli & Walter 2013), $R_{31} = 0.5$ adopted by Tacconi et al. (2013), $R_{41} = 0.25$ from the R_{31} value and the measured ratio $R_{43} = 0.54 \pm 0.15$ for DYNAMO $z = 1 - 2$ MS analogue sample (Lenkić et al. 2023). We then convert the CO(1-0) flux luminosity to total molecular gas mass with $\alpha_{\rm CO} \sim 0.8$ for both SMG and QSO and $\alpha_{\rm CO} \sim 4.36$ for normal MS star-forming galaxies. We assumed 40% uncertainty on high-J to CO(1-0) conversion, 40% on $\alpha_{\rm CO}$, and statistical uncertainty of the flux, finding the total uncertainty on the molecular gas mass in root-sum squared. The mean uncertainty derived is 60%, consistent with the assumed systematic uncertainty of 50% used in Tacconi et al. (2013).

The value of $\alpha_{\rm CO}$ is inferred to be consistent with the Milky Way value for normal star-forming galaxies and much less for ULIRGs, SMGs, and QSOs based on dynamical arguments (Tacconi et al. 2008; Hodge et al. 2012). The works calibrating the conversion factor including dust measurements also suggest similar trends, and relatively small values for galaxies above the main sequence (Genzel et al. 2015).

For galaxies with available [C I] (1−0) and [C II] flux measurements but without CO measurements, we assume that these line fluxes are molecular gas mass tracers, with the conversion factors $\alpha_{\rm CI} = 17$ with 20% uncertainty based on calibration by Dunne et al. (2022), and conversion factor by Zanella et al. (2018), $M_{\rm mol}/L_{\rm [CII]} = 30$ with 50% uncertainty. For the gravitationally lensed systems, we used the reported intrinsic luminosity after correcting the lensing magnifications (Rizzo et al. 2021; Fujimoto et al. 2024).

There can be large uncertainties associated with molecular mass measurements resulting from unknown metallicity and dust dependencies (see, e.g., Eales et al. 2023). In this study, we do not include any possible variation in the conversion factor due to metallicity which is unknown for the majority of the sample.

We also cross-match the ionised gas data compilation at cosmic noon with published molecular gas or dust measurements from Liu et al. (2019a), Tadaki et al. (2020b), Kaasinen et al. (2020), and Adscheid et al. (2024). A total of 11 matches were identified and homogenised as described above.

The distribution of the total sample, including the optical, FIR, and millimeter literature compilations, is shown by by black histograms in Fig. 1. Parameters include redshift, star formation rate, stellar mass, offset from the main sequence, molecular gas mass, and disc velocity dispersion. The offset from the main sequence (ΔMS) is measured with respect to the main sequence defined by Speagle et al. (2014) for consistency with Section 3.3. The full sample is representative of the massive galaxy population at these redshifts (e.g., median ΔMS = −0.09, median $\log[M_*] = 10.4$). The subset of galaxies with estimated molecular gas masses, 26%, are over-plotted in blue. This subset spans the full range of redshift and velocity dispersions but is concentrated at higher star formation rates, higher stellar masses, and to on or above main sequence galaxies (median ΔMS= 0.34)

reflecting the demanding molecular gas line observations for low mass systems.

2.3 Kinematic measurement techniques

Kinematic properties, specifically disc velocity dispersion (σ) and rotational velocities (V), have been measured differently across the literature. While some works measure values from 1D or 2D fits and apply a beam smearing correction, others use forward modelling techniques applied to the 3D data cubes. Beam smearing corrections and modelling codes rely on underlying assumptions of the kinematics (e.g. rotation model, radial variation in dispersion) that also vary across the literature. For the purposes of this work we have not attempted to homogenise methods. This undoubtedly results in a higher scatter in the combined dataset (e.g., Davies et al. 2011). It is beyond the scope of this paper to re-fit all kinematic results in the literature at the cube level with the same kinematic tool and or methods. Future work will employ a non-parametric model to available public IFU data (Kanowski et al. *subm*).

Some investigations have shown comparisons between measurement techniques (e.g., Davies et al. 2011; Varidel et al. 2019; Parlanti et al. 2023; Lee et al. 2024a) however the comparisons are subject to model input and data quality, including S/N, spatial resolution, spectral resolution, error handling, etc.. We show the variety of measurement techniques and emission lines of the full data compilation in the next Section.

Finally, we note that while most codes seem to agree when extracting observed velocities, inclination uncertainties can have a large impact on derived rotational or circular velocities (where rotational velocity is the observed velocity corrected for inclination and beam-smearing and circular velocity also includes a pressure-support term). Inclinations are typically derived from the highest resolution imaging available, which can range from *JWST* to the kinematic data itself. For galaxies with only a few resolution elements, it is difficult to accurately constrain the structural morphology, especially if galaxies are thicker or more triaxial at early times (e.g., van der Wel et al. 2014; Elmegreen et al. 2017; Hamilton-Campos et al. 2023).

3 RESULTS AND ANALYSIS

We plot the dispersion measurements as a function of redshift for the full literature compilation in Fig. 2. Each panel shows the compilation color-coded by different observational or technical characteristics to highlight the heterogeneous nature of the sample. The same figure is reproduced in Fig A1 as a function of lookback time, rather than redshift, and with dispersion visualised on a linear scale. There is a clear split with redshift with regards to which gas tracer is predominately measured. Observations with *JWST* will reduce this bias for ionised gas observations at $z > 4$, however with current mm/sub-mm facilities the the same line can not be used to trace molecular gas across the full redshift range. While we do not see an obvious bias introduced by the different codes used in this heterogeneous dataset, Fig. 2 (bottom), some works have made direct comparisons and found systematic offsets, e.g., Parlanti et al. (2023); Lee et al. (2024a). We denote measurements from sources that are gravitationally lensed with a star in the bottom panel.

The results show considerable scatter around a median of 40 km s^{-1}, with little evolution between $z = 1$ to $z = 8$. The flat evolution of $\sigma_{\rm gas}$ has been seen at high redshift from other authors (Rizzo et al. 2023, 2024). However, it is in contrast to expectations of what would have been extrapolated from previous model assumptions (red hatched) extending to ~ 100 km s^{-1} at $z \sim 6$ (e.g., Lelli et al. 2023; Posses et al. 2023). This model, proposed in Wisnioski et al. (2015), hereafter, W15, built on Toomre (Toomre 1964) stability theory for disc galaxies. In this section we explore the model assumptions used in W15 and provide updated prescriptions for variables that evolve as a function of time. The updated model, described below, is shown by the gray band in Fig. 2 which shows better agreement with the full data compilation.

3.1 Toomre stability model

An assumption invoked to reconcile observations of high gas velocity dispersions in galaxies at $z > 1$ with theoretical expectations is that the gas is in a state of marginal gravitational stability parameterised by the Toomre parameter, Q, where

$$Q_{\rm gas} = \frac{\sigma_{\rm gas}\kappa}{\pi G \Sigma_{\rm gas}} \approx 1 \tag{1}$$

for a single phase of gas. Above, $\Sigma_{\rm gas}$ is the surface density, κ is the epicyclic frequency, G the gravitational constant, and $\sigma_{\rm gas}$ is the radial velocity dispersion of the gas. This simplified argument has been used to explain the evolution of gas velocity dispersion assuming isotropic (or radially constant) gas velocity dispersion (e.g., Genzel et al. 2011; Wisnioski et al. 2015) and the existence of large star-forming clumps at early times (e.g., Immeli et al. 2004; Genzel et al. 2011; Wisnioski et al. 2012). To directly compare with kinematic results, Genzel et al. (2011) derived the Toomre relation in the form of

$$Q_{\rm gas} = \frac{\sigma}{V}\frac{a}{f_{\rm gas}} \tag{2}$$

where a describes the rotation model with a values of 1, $\sqrt{2}$, $\sqrt{3}$, and 2 for a Keplerian, constant rotation velocity, uniform density, and solid body disk, and V is the rotational velocity, where $V = V_{\rm obs}/\sin(i)$ and i is the inclination. For simplicity, we do not make a pressure support correction (e.g., Burkert et al. 2010). To derive the mass-average evolution of dispersion over time t, $\sigma(t)$, $f_{\rm gas}(t)$ can be parametrised as

$$f_{\rm gas}(t) = \frac{1}{1 + (t_{\rm dep}(t){\rm sSFR}(t))^{-1}}, \tag{3}$$

where sSFR(t) is the specific star formation rates, $t_{\rm dep}(t)$ is the depletion time, and $f_{\rm gas}(t)$ is the gas fraction.

While this theory successfully reproduces a number of observations it is a simplification in many respects which are explored in the following sections. The assumption of $Q \approx 1$ in particular, and treatment of only a single phase of gas is discussed in Section 3.5. The use of this derivation is to relate the changing conditions of galaxies over cosmic time, e.g. more molecular gas and higher star-formation rates, to the apparent change in disc velocity dispersions over time. Given the heterogeneous nature of the data compilation in both quality and phase we do not explore more complex derivations of Toomre stability theory here (e.g. Wang & Silk 1994; Romeo et al. 2010; Romeo & Wiegert 2011; Nipoti 2023; Aditya 2023, 2024; Bacchini et al. 2024). A model exploration will be published in a future work (Leaman et al. in prep).

The main difference between the updated model (gray) and model from W15 (red) in Fig. 2 comes from the assumptions for the evolution of sSFR(t) and $f_{\rm gas}(t)$ or $t_{\rm dep}(t)$. Each of these has a secondary dependence on stellar mass. In W15, sSFR(t) and $f_{\rm gas}(t)$ were parametrised using Whitaker et al. (2014) and Tacconi et al. (2013) to $z \sim 2.5 - 3$, respectively. For the main body of this paper

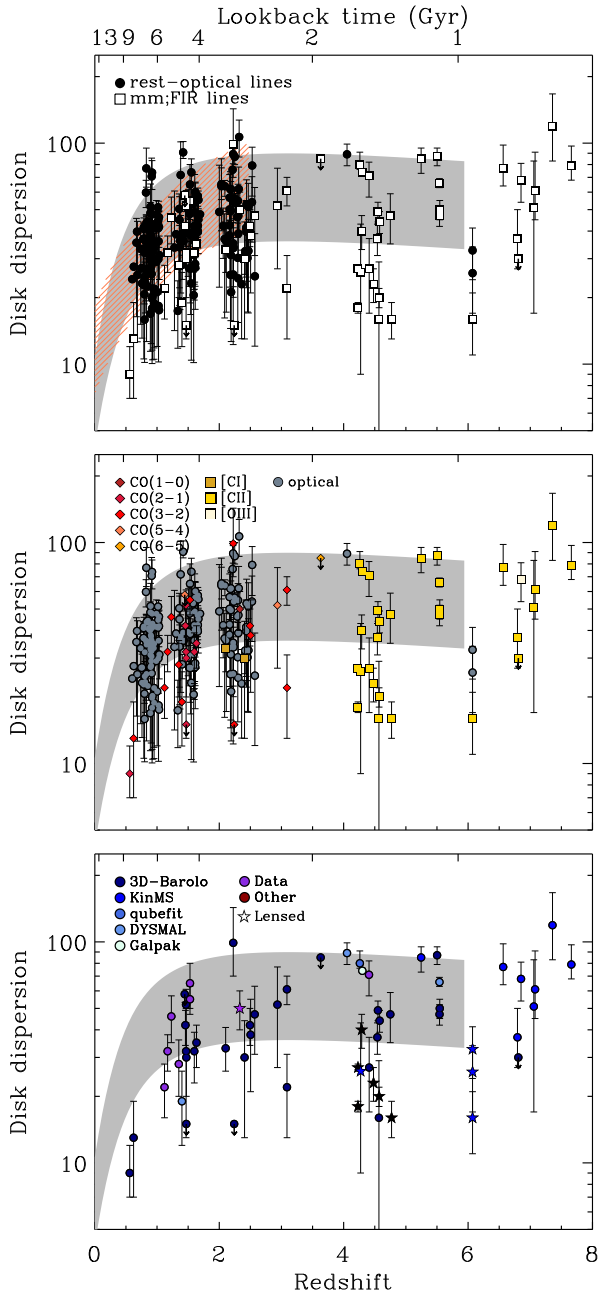

Figure 2. Ionised and molecular gas data compilation at $z > 0.5$ of disc velocity dispersion. *Top:* The black circles indicate measurements from ionised gas with primarily integral field spectroscopic data. The white squares indicate measurements from resolved molecular gas interferometric data. Upper limits in both cases are indicated with downward arrows. The gray and red bands show predictions from a simplified Toomre stability model. The gray band represents an update from W15 (red dashed) using more recent data-driven prescriptions for sSFR(z) and $t_{\rm dep}$(z). The bands are shown only at the redshifts which sSFR(z) and $t_{\rm dep}$(z) have been reliably measured. *Middle:* Same as the top panel with symbols coded by emission line. The [C I] and [C II] group includes [C I] (1-0) 609 μm, [C I] (2-1) 370 μm, and [C II] 158 μm lines. The [O III] group refers to the [O III] 88 μm FIR line. *Bottom:* Same as above, for mm/FIR sample, with symbols coded by kinematic extraction technique. Lensed galaxies are shown by stars while all other data are shown by circles. Purple points show measurements extracted directly from the data without using 3D modelling codes. We include data analysed with 3D modelling codes including, 3D-Barolo (Di Teodoro & Fraternali 2015), KinMS (Davis et al. 2013), qubefit, DYSMAL, and GalPak3D (Bouché et al. 2015).

we adopt Tacconi et al. (2020) for $t_{\rm dep}(t)$ and Speagle et al. (2014) for sSFR(t) (as used by Tacconi et al. 2020). We explore the different parameterisations of sSFR(t,M_*) and $t_{\rm dep}(t,M_*)$ in Sections 3.2 and 3.3.

3.2 The role of molecular gas & depletion time evolution

Large compilations of molecular gas estimates from the literature using emission lines from CO transitions and FIR fine structure lines as well as dust continuum measurements have been use to map the evolution of molecular gas properties across time, mass, and star-formation rates (e.g., Scoville et al. 2017; Tacconi et al. 2020; Liu et al. 2019b). A detailed comparison of molecular gas evolution is given in Liu et al. (2019b) and Dessauges-Zavadsky et al. (2020).

In short, differences in the evolution prescriptions can result from sample selection (e.g., z, M_*, SFR) and molecular gas tracers. The functions defined by Tacconi et al. (2018) and Scoville et al. (2017) are primarily derived using data from $z = 0-3$ and should therefore not be extrapolated, while Liu et al. (2019b) and Tacconi et al. (2020) extend to $z \sim 4.5$. Recent work by Dessauges-Zavadsky et al. (2020) at $z \sim 5-6$ with the ALPINE-ALMA survey of moderate mass ($M_* \sim 10^9 - 10^{10}$ M$_\odot$) galaxies using [C II], supports the extension of the Tacconi et al. (2018, 2020) results to $z \sim 6$. The evolution of gas fractions and depletion times do show some dependence on stellar mass which is seen in all the above works but is particularly pronounced in Liu et al. (2019b). In Liu et al. (2019b) the depletion time shows a reversal in slope towards lower masses. The derived evolution of depletion time and molecular gas fraction for different stellar mass bins are shown in the middle and right panels of Fig. 3 respectively.

Given the evidence that the equations in Tacconi et al. (2020) can be extended to $z \sim 6$ we adopt the depletion time scaling relation of equation 4 from Tacconi et al. (2020) which characterises depletion time as a function of redshift, stellar mass, and MS offset. The inclusion of offset from the star-formation main sequence (ΔMS) in $t_{\rm dep}(t,M_*)$ can change the normalisation of $t_{\rm dep}(z)$ but not the slope. Taking into account the MS term removes the need for a varying $\alpha_{\rm CO}$ for ΔMS. For simplicity we ignore this term assuming all galaxies are 'main sequence' galaxies. Most galaxies in the literature sample fulfil this criteria within errors as shown in Fig. 1. However the distribution has outliers and extends beyond 1 dex of the MS. Offsets from the MS could play a large role in terms of the amount of molecular gas present (e.g., Tacconi et al. 2020). For example, using ΔMS = [-0.5, 0.5] at logM_*[M$_\odot$]=10.5 would result in a factor of [0.5,1.4] in $f_{\rm gas}$ and σ. We explore some of our key results in Appendix B with respect to offsets from the MS.

We note that in this section we explore predictions for velocity dispersion of galaxies at fixed mass at different redshifts but the evolutionary pathways for *individual* galaxies is mass dependent. Today's most massive galaxies (in more massive halos; $M_{\rm halo} = 10^{14}$ at $z = 0$) likely had a relatively flat molecular gas fraction until $z \sim 2$ followed by a decline. In contrast, the evolutionary pathways of less massive galaxies (in $M_{\rm halo} = 10^{13}$ at $z = 0$) may have have a steep decline from $z = 5$ to $z = 0$ (Dessauges-Zavadsky et al. 2020). Another caveat is that we are using multiple gas tracers for the kinematics but focus on molecular gas fractions, as ionised gas does not significantly contribute to the disc mass. We discuss this in more detail in Section 4.2.1.

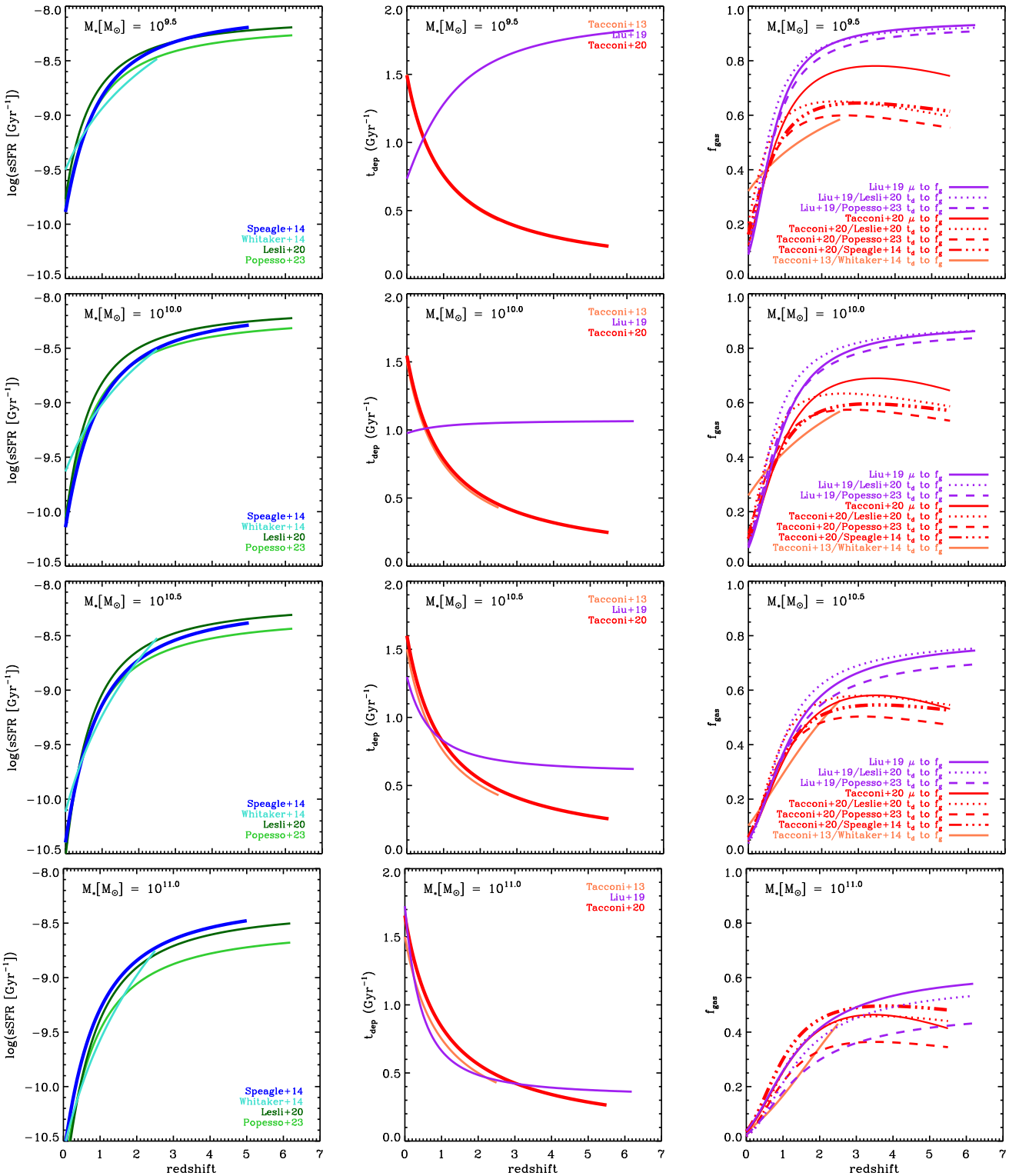

Figure 3. A sub-sample of commonly adopted evolutions of sSFR(z) (left), $t_{\rm dep}(z)$ (middle), and $f_{\rm gas}$ (right) at a stellar mass of log(M_*[M$_\odot$])=[10.0,10.5,11.0] from top to bottom respectively. Lines show the extent of the datasets used. For sSFR(z) (left) we include comparisons of Speagle et al. (2014), Whitaker et al. (2014), Leslie et al. (2020), and Popesso et al. (2023). Relations are extended to the maximum redshift of the data included in the respective samples. In the middle column we compare $t_{\rm dep}(z)$ prescriptions from Tacconi et al. (2013), Liu et al. (2019b), and Tacconi et al. (2020). We note that the different references adopt different SFR indicators which can also lead to differences in depletion times. In the right column we compare different derivations for the evolution of gas fractions. As described in Section 3.2, $f_{\rm gas}(z)$ can be derived using equation 1 or converting $\mu(z)$, where μ equals $M_{\rm gas}/M_*$, to $f_{\rm gas} = M_{\rm gas}/(M_* + M_{\rm gas})$. We assume the SFR/SFR(MS) = 1 for all included derivations for simplicity but note that the more recent derivations of $t_{\rm dep}$ and $f_{\rm gas}$ do include a dependency on offset from the main sequence. We do not include all possible literature derivations of these properties but pick a relevant subset to show the magnitude of differing assumptions. We adopt Speagle et al. (2014) for sSFR(t) and Tacconi et al. (2020) for $t_{\rm dep}$in the remainder of the paper and highlight these relations in a bold line.

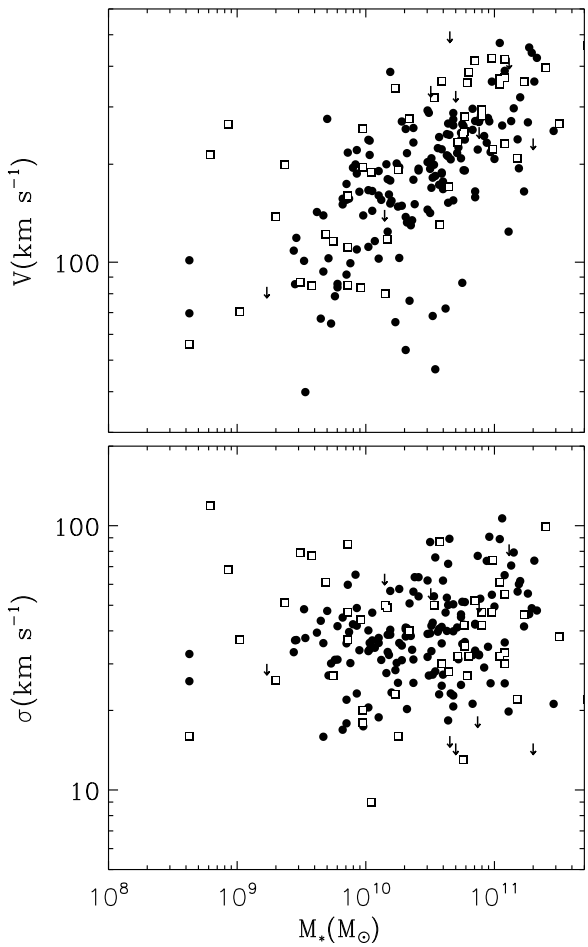

Figure 4. Inclination corrected rotational velocity, V, and disc velocity dispersion, σ, as a function of stellar mass, M_*, for the data compilation. Ionised gas tracers are shown as black points and the FIR/sub-mm sample is shown with open squares. While there is a clear correlation for V-M_*(Pearson correlation, $r = 0.72$), reflective of the Tully-Fisher relation, there is no correlation for σ-M_*(Pearson correlation, $r = 0.07$), however we note here that σ from the observations is the line-of-sight velocity dispersion.

3.3 The role of specific star formation rate evolution

In comparison to depletion time or molecular gas content, SFRs are far easier to estimate for large galaxy populations. However, due to the number of techniques used to estimate SFR and the variety of data quality, it can be difficult to measure the evolution of sSFR consistently across all of cosmic time. Large compilations spanning wide redshift and mass range include Speagle et al. (2014), Leslie et al. (2020), Thorne et al. (2021), and Popesso et al. (2023). The exact shape is influenced by the SFR indicator used, how star-forming and passive galaxies are separated, observational biases etc. (e.g., Leja et al. 2022). In the left panels of Fig. 3 we show the comparison of different sSFR(z) parameterisations in four different stellar mass bins. Despite the challenges mentioned, the different parameterisations for sSFR are in good agreement across $10^{9.5} - 10^{11}$ M$_\odot$with some minor normalisation differences which are more pronounced in the highest mass bin. The slope of the evolution of Whitaker et al. (2014), used in W15, is marginally steeper than the other parameterisations between $z = 0 - 3$ at all masses.

For this work we adopt the sSFR(z) from Speagle et al. (2014) for consistency because it was used in deriving the evolution of depletion time and molecular gas mas in Tacconi et al. (2020). The last column of Fig. 3 shows how $f_{\rm gas}(z)$ and therefore $\sigma(z)$ would change if we use different observationally-derived prescriptions for the evolution of sSFR(z) and $t_{\rm dep}(t)$ together. There is a significant normalisation difference particularly at low mass ($M_* < 10^{10}$M$_\odot$) and high redshift ($z > 3$). This difference may be due to low number statistics in this regime in deriving both sSFR(z) and $t_{\rm dep}(z)$. The steepness in the $\sigma(t)$ model from W15, red band in Fig. 2, can be seen here as directly related to the use of the sSFR(z) from Whitaker et al. (2014). Interestingly, at $z > 3$ the derivations using Tacconi et al. (2018, 2020) with Leslie et al. (2020); Popesso et al. (2023) show a turn-over to lower $f_{\rm gas}(z,M_*)$, and therefore lower $\sigma(z,M_*)$, to higher redshifts.

3.4 Stellar mass assumptions

As discussed in Section 3.2 and Section 3.3 and shown in Fig. 3, the shape and normalisation of the derived model of $\sigma(z)$ is dependent on stellar mass. For Fig. 2 we assume an average mass, log M_*[M$_\odot$] = 10.5, which matches the mean of the full sample. However, given the wide range of M_* covered by the data compilation, we explore the dependence of the data compilation and updated model on M_* in Fig. 4 and Fig. 5. The ionised gas sample spans the whole mass range with the highest concentration of galaxies at log M_*[M$_\odot$] = 10−11. In contrast the mm/FIR sample more uniformly spans the full mass range. It is possible that disc dispersions correlate with stellar mass either directly or indirectly through secondary correlations (e.g., SFR-M_*, V/σ-M_*). In Fig. 4 we show the σ and V as a function of stellar mass. While there is a clear correlation between V and M_*, as expected by the Tully-Fisher relation, there is no strong correlation between σ and M_*. This has been previously explored in the ionised gas data in Übler et al. (2017) and Übler et al. (2019).

The expected evolution using Toomre stability arguments is shown with gray lines for appropriate choices of rotational velocity for each mass bin in Fig. 5. A steeper population evolution is predicted at high mass than at low mass, specifically with respect to $z = 1 - 4$, as expected from the right panels of Fig. 3. The majority, approximately two thirds, of the ionised gas data overlaps with the model expectations for the full mass range, with better agreement in the lowest (log(M_*[M$_\odot$]) = 8.5 − 9.5) and highest (log(M_*[M$_\odot$]) > 11) mass bins, although those have the lowest number statistics. In contrast the millimeter data compilation is mostly below the model expectations, except at log(M_*[M$_\odot$]) < 10.0, which may indicate a difference in the kinematics between phases (e.g., Übler et al. 2019; Girard et al. 2021). We explore the differences in σ between gas phases in Section 4.2.1.

3.5 Other model assumptions

The Toomre model also includes the variables a, V, and Q. For comparison to the literature dataset, a value or range has been assumed. We explore those choices here. The exact geometry of the galaxies considered has implications for the assumed value of the constant a. In W15 and in this work we assumed $a = \sqrt{2}$. The choice of a can have an effect of up to a factor of 2 on the expectation from equation 1.

The width of the model band is determined by a range of circular velocities. Due to the relatively tight correlation between mass and velocity (e.g., Tully & Fisher 1977; Tully & Fouque 1985; McGaugh et al. 2000) the choice of V should reflect the appropriate range

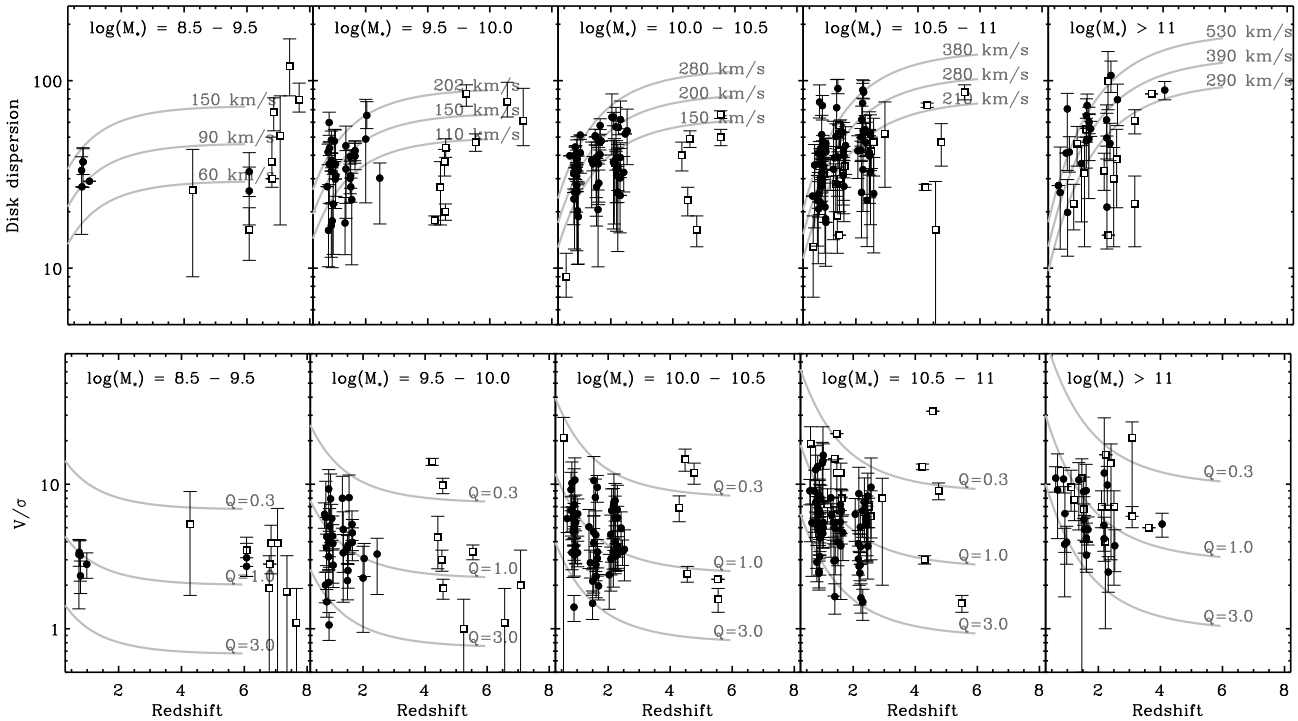

Figure 5. Gas velocity dispersion (top) and the ratio or gas rotational velocity to velocity dispersion in stellar mass bins. The data are the same as Fig. 2, optical (black circles) and FIR/mm (open squares). The analytic prescription, described in Section 3, is shown for different rotational velocities (top panels) and Toomre Q parameters (bottom). The rotational velocities chosen represent the range expected for each mass bin given the $z \sim 1-2$ Tully-Fisher relation and intrinsic scatter defined in equation 2 and Table 2 of Übler et al. (2017) respectively.

based on the range of stellar masses for the dataset. For Fig. 2 we use $100-250$ km s^{-1}. The top panels of Fig. 5 show three curves reflecting appropriate rotational velocities assuming minimal evolution of the stellar Tully-Fisher relation from $z \sim 1-8$ using Übler et al. (2017) in mass bins of 0.5 dex. The majority of data fall between the expected rotational velocities but a significant fraction of data, particularly the mm/FIR measurement, across all redshifts scatter to lower dispersions. The majority of mm/FIR measurements (white squares) that have measured dispersions lower than the expectation, shown by the lowest gray line, actually have corresponding rotational velocities that are much higher than expected by the model (up to 500 km s^{-1}), indicative of a high V/σ and/or much lower Q.

The measured V/σ are explored in the bottom panels of Fig. 5 with model lines for $Q = 0.3, 1.0, 3.0$. In comparison to Fig. 2 and the top panels of Fig. 5 these panels take into account an extra observable, V. A wide range of V/σ values, from $\sim 1-20$, are seen in the literature across all stellar masses, consistent with model expectations of $Q \sim 1$ on average. The increasing model values of V/σ with M_* reflects the decreasing fraction of $f_{\rm gas}$ with M_*. In the data, V is strongly correlated with M_* (as expected by the Tully-Fisher relation; Fig. 4) while σ shows no correlation with M_*.

For thin disks, $Q = 1$ is the commonly used critical value to define marginal stability (Binney & Tremaine 2008). This assumes a single phase infinitesimally thin disc. However, it is well know that galactic discs are composed of multi-phase gaseous components probed by HI and H_2, HII regions and young stars, and old stars. Theoretical works have shown that the global stability of the multi-phase disc can differ from the stability of any one individual phase. In particular, some simulations (Renaud et al. 2021) show that locally HI discs can have higher Toomre stability parameters of $Q_{\rm HI} \gtrsim 10$, molecular discs have $Q_{\rm H_2} \sim 10$ and stellar discs have $Q_* \sim 1-3$ (Westfall et al. 2014). In contrast, Fig. 5 (bottom) shows that the cooler gas tracers (mm/FIR lines) are consistent with $Q \lesssim 1$. A low Q parameter, $Q \sim 0.3$, has been noted in high redshift clumpy cool gas disks (Fujimoto et al. 2024). Assuming different combined values of Q would change the normalisation of the expected evolution of disc velocity dispersions.

An additional complication is that the Toomre arguments used here assume a infinitesimally thin disc, which is an unjustified assumption for the majority of the data in this compilation (Elmegreen & Elmegreen 2006; van der Wel et al. 2014; Elmegreen et al. 2017; Lian & Luo 2024; Tsukui et al. 2024)[1]. Theoretical derivations of disc stability criteria of thick discs imply a lower value of $Q_{\rm crit} \sim 0.7$ (Kim et al. 2002; Bacchini et al. 2024). The formalism introduced by Romeo & Falstad (2013) includes both a term that accounts for the stabilisation effect due to finite thickness as well as a weights for each component. The reduction in $Q_{\rm crit}$ would result in a lower expectation for σ bringing the gray band in Fig. 2 closer to the lower envelope of measurements.

[1] An additional complication of the Toomre formalism used here is whether the scale that the dispersion is measured at is above or below the scale height of the disc (Renaud et al. 2021). Because the observations utilised can not independently measure these two parameters we are unable to consider a more precise formalism

4 DISCUSSION

4.1 Shape of the evolution

While ionised gas results indicated a steady evolution between $z = 0.5 - 2.5$ (e.g., Simons et al. 2017; Wisnioski et al. 2019, recent work has claimed no evolution in V/σ between $z = 0.5 - 3.5$ (Rizzo et al. 2023), meanwhile other works have suggested discs at $z \sim 4 - 8$ are dynamically colder than expected (Rizzo et al. 2020; Lelli et al. 2023). The expected shape of the evolution of dispersion at fixed mass is most strongly tied to the co-evolution of gas fractions and sSFR at fixed mass (Fig. 3, Fig. 5). As a result, the expectation of the shape of evolution beyond $z \sim 4$ is still uncertain with fewer measurement constraints on gas fraction across a wide mass range. Using updated prescriptions for the evolution of depletion time and specific star formation rates, the expected evolution of disc dispersions would flatten beyond $z \sim 1$, with a mild dependence on stellar mass. Fig. 5 shows that a smaller difference in measured disc dispersions is expected as a function of cosmic time for low mass systems compared to high mass systems. This could be linked to the 'disc settling' scenario (Kassin et al. 2012; Tsukui et al. 2024) in which galaxies generally settle as they become more massive and from $z \simeq 1$ experience less mergers and accretion with cosmic time (e.g., Wisnioski et al. 2019). A similar shaped evolution has been derived using a purely feedback driven model (Rizzo et al. 2024) with dependencies on disc scale height, molecular gas mass and total star-formation rates.

Fig. 2 and Fig. 5 reveal that most literature results of σ at kpc-scales at $z > 4$ are consistent with theoretical predictions from marginal stability arguments, with considerable scatter towards lower dispersions. This is best seen in Fig. 5, where it becomes clear that the gas phase used for measurement may also have an effect on the measured dispersions and stability, as discussed in Section 3.4 and explored more in Section 4.2.1.

The evolution at fixed mass has a self-similar shape to the recently measured evolution of disc thickness for low-mass edge-on galaxies in *JWST* images ($\log(M_*[\mathrm{M}_\odot]) = 8.5 - 10.5$) from $z \sim 5 - 0$ (Lian & Luo 2024). In that study, a flat evolution is measured between $z \sim 3 - 1$ of ~ 0.4 kpc with 1σ scatter of 0.15 kpc and a decline to ~ 0.2 kpc at $z = 0$ (but see Tsukui et al. 2024). Together, these results suggest, that at least for low masses, discs can form in a thick configuration at early times or become thick quickly. Dynamical 'heating' likely occurs from a number of processes after formation contributing to the scatter in the thickness of stellar discs. Once thick, subsequent minor mergers or secular processes become dynamically inefficient with only major mergers possible to remove the existing thick disk.

The simple model does not show the evolution of individual galaxies but likely captures the population average at various redshifts due to minimal evolution of the sSFR and f_{gas} relations beyond $z \simeq 1$. Pathways of individual galaxies should be varying significantly in diverse ways due to their varied star formation and merger histories.

4.2 Scatter

While the global evolution of mass averaged measurements can be modelled using Toomre stability theory, the scatter at any given epoch reflects the combination of internal physics driving the pc-scale motions in the ISM as well as systematic uncertainties (resolution effects, tracer, measurement methodology). What physical mechanisms drive and maintain disc-scale turbulence across cosmic time remains an elusive problem due to the combination of systematic uncertainties (e.g., Johnson et al. 2018; Übler et al. 2019). In this work we find no direct dependency on stellar mass, though secondary correlations could exist due to the connection between stellar mass and gas fractions or more massive galaxies becoming more stable (e.g. $Q > 1$).

How the scatter of kinematic measurements relates to the molecular gas reservoir through measurements of M_{gas}, f_{gas}, and/or t_{dep} has been particularly observationally challenging. Large statistical studies of multi-phase tracers have not been obtained. These limitations motivate using the large but heterogeneous literature compilation presented in Section 2. In the following sections, we utilise the smaller sub-sample of 63 galaxies with both kinematic and gas reservoir estimates.

4.2.1 *Offset between gas phases*

Using the homogenised M_{gas} values described in Section 2, we directly compare the velocity dispersion with measurements of M_{gas}, f_{gas}=M_{gas}/(M_{gas}+M_*), and t_{dep}=M_{gas}/SFR independent of redshift. Fig. 6 (left) shows the dispersion as a function of M_{gas} color-coded to indicate which gas phase is being used to trace the kinematics. For ionised gas tracers we include data from rest-optical lines (Hα, [O III] 5007Å) and rest FIR line [O III] 88μm (which traces HII regions around young stars; Ward et al. 1975; Rubin 1985). For molecular gas tracers we include data from CO transitions as well as [C I] 370μm, [C I] 609μm. There has been both theoretical and observational evidence that [C I] traces molecular clouds similar to low J CO transitions (e.g., Ikeda et al. 2002; Alaghband-Zadeh et al. 2013; Clark et al. 2019). We do not classify [C II] 158μm as either ionised or molecular gas tracer as it is found in regions of ionized, molecular, and neutral gas over a large range of temperatures (e.g., Goldsmith et al. 2012; Pineda et al. 2014).

From the left panel of Fig. 6 we see a separation between ionised and molecular gas dispersions at fixed M_{gas}, such that ionised gas tracers (orange) cluster to higher dispersions than molecular gas tracers (blue). Expectations from Toomre stability theory are included for $Q = 0.3$ and $Q = 0.67$, assuming a 50% molecular gas fraction and that the Tully-Fisher relation holds and does not evolve significantly at high redshifts. While the data sample is limited to high gas masses, the data are not inconsistent with the model expectation. As expected from Fig 5, the molecular gas dispersions align better with the $Q = 0.3$ model while the ionised gas dispersions align better with the $Q = 0.67$ model. These results indicate that high dispersions of $\sim$50 km s^{-1} can be reached in the molecular phase but only in highly unstable disks with large gas masses of $> 10^{11}\mathrm{M}_\odot$. Ionised gas dispersions are higher by a factor of ~ 2 on average at fixed gas mass. This offset is comparable to a similar offset seen in σ, for fixed gas fraction, for a compilation of local analogs of galaxies at cosmic noon (high SFRs, higher velocity dispersions) that have measurements for the same sources in *both* CO and Hα (Girard et al. 2021). We do not see as clear of an offset when considering σ as a function of f_{gas} as shown in the middle panel of Fig. 6. It is possible this reflects the uncertainty in the measurements (e.g. M_*) or could imply that the gas reservoir is more fundamental in setting the dispersion.

Some of the offset seen may result from the different methods typically used to measure dispersion across samples. As shown in Fig. 2, 3D-Barolo is favoured for studies of mm/FIR, while other methods are favoured for optical data. Lee et al. (2024a) show that in low S/N data dispersions can be underestimated in the outskirts using non-parametric codes. Further studies are required to measure the magnitude of this effect in the current data.

At $z = 0.6 - 2.7$ the scatter in rest-frame optical dispersions was explored with relation to M_{gas} and f_{gas} (Übler et al. 2019), with the molecular gas properties derived from scaling relations (Tacconi et al. 2020). The correlations between σ-M_{gas} and σ-SFR were shown to

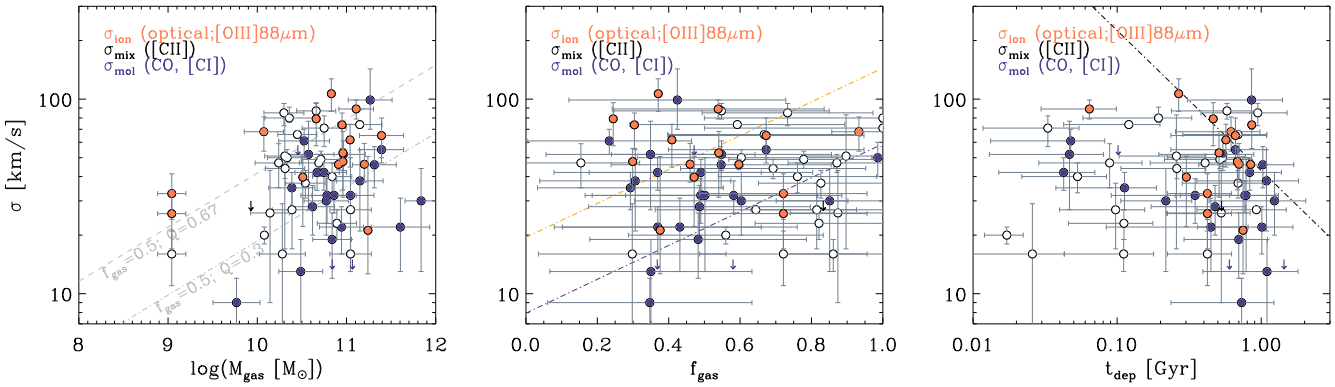

Figure 6. Velocity dispersion as a function of molecular gas properties: $M_{\rm gas}$, $f_{\rm gas}$, $t_{\rm dep}$ from left to right for galaxies with a molecular gas mass, stellar mass, and SFR measurement. Galaxies are color coded by gas phase. Orange points represent galaxies with kinematic measurements of rest-frame optical emission lines (Hα, [O III]) and the [O III] 88μm line. Dark blue points represent galaxies with kinematic measurements of cooler gas tracers including CO transitions and [C I] 370μm, [C I] 609μm. Open white symbols represent galaxies with kinematic measurements from [C II] 158μm a mixed gas phase tracer. Dashed lines in the left panel show equation 2 assuming the (Übler et al. 2017) Tully-Fisher relation, a molecular gas fraction of 50% and $Q = 0.3, 0.67$. The dot-dashed lines in the middle panel show fitted relations from Girard et al. (2021). The dot-dash line in the right panel shows the fit to local data from Fisher et al. (2019) consistent with the multi-freefall turbulence models of Salim et al. (2015). Arrows represent upper limits of the dispersion. Errors show propagated uncertainties assuming a 0.3 dex error on stellar mass measurements and a 30% error on SFR measurements.

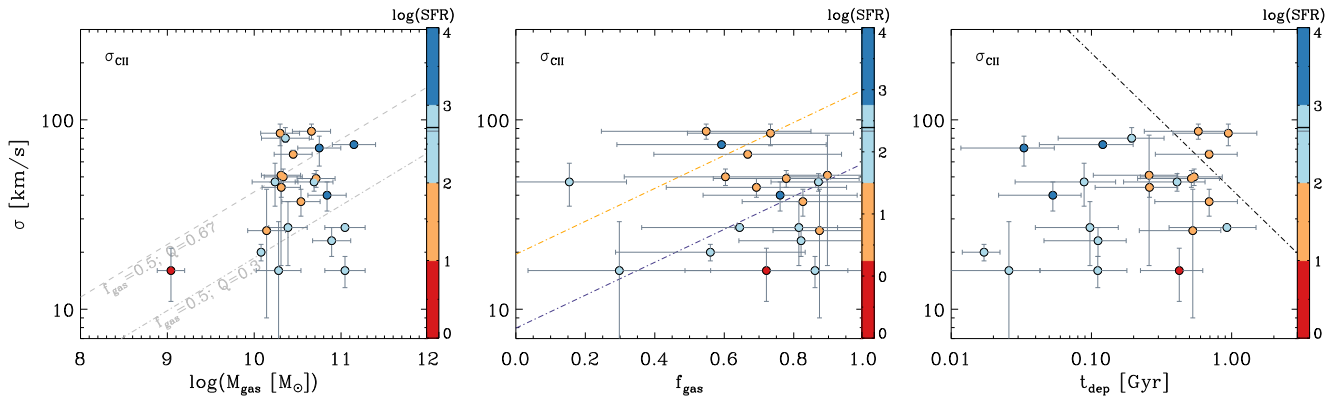

Figure 7. Same as Fig. 6 but showing only kinematic measurements derived from [C II] . Color coding represents measured star formation rates as denoted by the color bars. Star formation rates are taken from multiple tracers depending on the observations available as described in Section 2.

have equal Spearman rank coefficient ($\rho_{\rm s} = 0.38$) and significance ($\sigma_\rho = 4.6$) with σ-$f_{\rm gas}$ showing only marginal significance ($\rho_{\rm s} = 0.12$; $\sigma_\rho = 1.4$). However, when the evolution of these parameters were taken into account the correlations became less significant. If we overlay the ionised gas σ and derived $M_{\rm gas}$ values from Übler et al. (2019) they overlap with the orange data points in the left panel of Fig. 6 but with higher scatter, likely induced by the derivation of $M_{\rm gas}$ from scaling relations. At higher redshift, $z = 4 - 7$, Parlanti et al. (2023) compile a sample of 36 galaxies, also included in this work, and find no correlation with $f_{\rm gas}$, suggesting a more direct dependence on dust mass or stellar mass.

Offsets in the dispersion of the warm ionised medium and cold neutral medium have also been seen in idealised ISM simulations (Rathjen et al. 2023) as a function of $\Sigma_{\rm SFR}$ due to stellar feedback (a factor of 2.2×, consistent with the offset seen by observations in Girard et al. 2021 and in Fig. 6). An offset of ~ 3× was identified in a larger sample of highly star-forming galaxies over $0 < z < 5$ (Rizzo et al. 2024). Together these results are suggestive of a coexistence of molecular and ionized gas discs with unique stability criteria. However, it does not necessarily follow that all disks are born with a 'cold' molecular disk. Differences in gas phase are also seen in isolated disc and zoom-in simulations (Ejdetjärn et al. 2022; Kohandel et al. 2024) with $\sigma_{\rm molecular} < \sigma_{\rm ionised}$. In these simulations, gas-rich discs ($f_{\rm gas}$~ 50%) are able to reach levels of molecular gas turbulence of up to 50 km s^{-1} (also seen in Fig. 6) without any stellar feedback. In these isolated disc simulations and in cosmological simulations (Orr et al. 2020), stellar feedback is responsible for the larger ionised gas dispersions or larger scatter, similar to the ISM slab simulations (Rathjen et al. 2023), while molecular gas turbulence is more closely linked to how galactic discs regulate their gravitational stability. Therefore the commonly measured ionised gas disc dispersion is dependent both on how turbulent the molecular gas was that the young stars were born from as well as the amount of star-formation feedback.

A weak trend is also seen when considering the relationship between velocity dispersion and depletion time (Fig. 6; right). The ionised and molecular gas measurements form overlapping populations close to the expectations from multi-freefall turbulence models

from Salim et al. (2015) and explored in Fisher et al. (2019) using local highly star-forming galaxies. Other models based on feedback-regulated star-formation predict a similar relationship but with a different slope. The data and errors do not justify a distinction between models. While the data compilation presented here does offer some insights into the turbulent nature of different components of the ISM, a dedicated program exploring multiple ISM tracers in the same galaxies is needed to confirm these results.

4.2.2 *Combining [C II] measurements together with other tracers*

Due to the brightness of the line, [C II], has become a popular tracer to explore $z > 4$ galaxy kinematics (Neeleman et al. 2020b; Rizzo et al. 2020; Tsukui & Iguchi 2021; Lelli et al. 2021; Rizzo et al. 2021), SFRs (e.g., Pineda et al. 2014; Herrera-Camus et al. 2015; Liang et al. 2024), and gas masses (e.g., Zanella et al. 2018; Dessauges-Zavadsky et al. 2020). The relatively low dispersion values measured with [C II], indicating dynamically 'cold' discs, at $z > 4$ (Neeleman et al. 2020b; Rizzo et al. 2020) are surprising given the more turbulent ionised gas results at $z \sim 1-3$ (Law et al. 2009; Förster Schreiber et al. 2009; Kassin et al. 2012; Wisnioski et al. 2015). A possible explanation has been that stars are born out of low-dispersion material, traced by the [C II], and star-formation driven feedback increases the dispersion, which is preferentially seen by the ionised gas measurements (e.g., Kohandel et al. 2024). In this data compilation, the kinematic measurements from [C II] span the range of ionised and molecular gas sequences in Fig. 6 with large scatter. Below we explore possible explanations including physical reasons and measurement uncertainty.

In Fig. 7 we isolate galaxies with kinematic measurements from [C II], and explore the possible role of a SFR dependence on the phase of gas probed by [C II] and thus reflected in the kinematics. The left panel of Fig. 7 shows that, at fixed $M_{\rm gas}$, disc dispersion is lower on average for galaxies with higher SFRs for the [C II] kinematic sample. This is contrary to expectations from arguments of star-formation driven turbulence seen in both theory (Faucher-Giguère et al. 2013; Krumholz & Burkhart 2016; Krumholz et al. 2018) simulations (Hung et al. 2019; Orr et al. 2020; Ejdetjärn et al. 2022; Jiménez et al. 2023) and observations (e.g., Lehnert et al. 2009; Green et al. 2010; Übler et al. 2019). The galaxies with SFRs < 100 M$_\odot$ yr^{-1} are on the upper envelope of the $\sigma - M_{\rm gas}$ trend seen in Fig. 6. If the result of a kinematic offset in phase discussed above is robust (noting the caveats in Section 2.2), and not dependent on stellar mass (Fig. 4), then these results indicate that [C II] traces a higher fraction of molecular gas in galaxies with high SFRs and primarily traces the warm ionised phase when SFRs are low/average.

This inference is consistent with some theoretical works and cosmological simulations that suggest molecular gas dominates the [C II] emission at high SFRs (e.g., > 20 M$_\odot$ yr^{-1}) or SFR densities (e.g., $\Sigma_{\rm SFR} > -0.5$ M$_\odot$ yr^{-1} kpc^{-2}), while atomic gas or gas in photo-dissociated regions (PDRs) takes over at lower SFRs and SFR densities (Olsen et al. 2015). The change with SFR density is suggestive that [C II] traces mostly molecular gas in high-density/pressure regions, and otherwise traces the atomic/PDR gas phase (Narayanan & Krumholz 2017). We do not explore the relation with SFR density in the data compilation due to large uncertainties in size measurements in the high redshift data.

Simulations (e.g., Liang et al. 2024; Gurman et al. 2024) and observations (e.g., De Looze et al. 2014; Herrera-Camus et al. 2015; Croxall et al. 2017) have explored the possible metallicity dependence of the [C II]–SFR relation which could also play a role in how best to interpret which phase is dominating [C II] kinematics. Gurman et al. (2024) find that the fraction of [C II] emission originating in ionized gas increases with galaxy metallicity, consistent with some observations (Croxall et al. 2017; Madden et al. 2020). In contrast, in the FIRE simulations (Liang et al. 2024) the fractional contributions of [C II] emission from different phases only depends strongly on metallicity above solar metallicities but shows a stronger dependence on depletion time at higher redshifts where metallicities are low. The very low depletion times of the high SFR sample in Fig. 7 (right) are associated to 20-40% molecular fractions of the [C II] in the FIRE simulations.

We are unable to explore the relationship directly with metallicity as most sources with [C II] detections do not have metallicity measurements as well. However, focusing on galaxies at a fixed gas mass of $M_{\rm gas} = 10^{10} - 10^{11}M_\odot$ in the left panel of Fig. 7 and assuming either the fundamental mass metallicity relation (Mannucci et al. 2010) or the gas mass metallicity relation (Bothwell et al. 2016) the galaxies with high star-formation rates (low dispersions) should have lower metallicities. This goes in the direction expected from [C II] studies that suggest molecular gas is traced well by [C II] in low metallicity (low dust) regions (Madden et al. 2020).

An alternative explanation for the spread in [C II] measurements is that the gas masses derived from dust continuum and rest-frame FIR lines for the highly star-forming galaxies are overestimated by roughly an order of magnitude. Cortzen et al. (2020) study the dust temperature of GN20, a galaxy within our sample (Übler et al. 2024b) finding that, assuming a constant gas to dust ratio, a dust temperature of 25 K verses 50 K could result in a 7× over-estimate of the gas mass. A reduction in the gas masses of the high SFR galaxies would bring them more in line with the lower SFR galaxies in Fig. 7 (left and middle). However, a reduction in $M_{\rm gas}$ for the high SFR galaxies would also lead to further reduction in the depletion time, in contrast to expectations from theory and observations (right).

The [C II] measurements at $z > 4$ are a key tracer available to measure gas dynamics with high accuracy due to the brightness of the line. While *JWST* will increasingly be able to explore the ionised gas dispersions (e.g., de Graaff et al. 2024; Nelson et al. 2023a; Übler et al. 2024b; Barišić et al. 2024; Danhaive et al. 2025) the NIRSPEC IFU and microshutters have a limited spectral resolution, uncertain line spread function (de Graaff et al. 2024), and difficult PSF (D'Eugenio et al. 2024). Therefore it is critical for dynamical studies to better understand the origin of [C II] in individual sources for comparison to existing literature.

5 CONCLUSIONS

We present a literature compilation of molecular and ionised gas kinematics at $z = 0.5 - 8$ of 237galaxies hosting rotation. The sample spans four orders of magnitude in stellar mass, four orders of magnitude in star formation rates, and three orders of magnitude in molecular gas mass. The data come from ground and spaced based optical and near-infrared integral field spectrograph observations, ground-based millimeter interferometer observations, and new *JWST* NIRSPEC observations. We find that kinematic measurements from far-infrared lines (traced by velocity dispersion, σ, and rotational support, V/σ) at $z > 4$ show significant scatter at fixed redshift comparable to ionised gas results at $z < 4$ likely dominated by the heterogeneous nature of the sample in data quality and galaxy properties.

Using the large literature compilation we explore the evolution in σ, V/σ, and Toomre stability, Q, from $z = 0.5 - 8$ finding no evolution in σ within the errors between $z \sim 1$ and $z \sim 8$. This

is consistent with simplified single component Toomre stability arguments in which the average evolution of gas dispersion at fixed mass is not expected to evolve significantly. While previous work, Wisnioski et al. (2015), presented a model that indicates a continually increasing dispersion with redshift if extrapolated, we present an updated model that predicts little evolution between $z = 6$ and $z = 2$ except in the highest mass bin ($\log M_*[\mathrm{M}_\odot] > 11$). This is confirmed, with considerable scatter, by the data compilation out to $z \sim 8$. We explore the effects on the expected average dispersion evolutions from different empirically derived evolution for gas fractions, depletion time, and sSFRs.

We identify a $\sim 2\times$ offset between velocity dispersion measured from molecular gas (as measured from CO, [C I] , and [O I]) and ionised gas (Hα, [O III]) at a fixed molecular gas mass, $M_{\rm gas}$, indicating a combination of physical processes driving a cooler molecular disc surrounded by a more turbulent ionised disc, consistent with previous literature compilations at lower redshifts and some zoom simulations. However, high values of dispersion in molecular gas discs (~ 50 km s^{-1}) are measured at high gas masses following expectations of a correlation between σ and $M_{\rm gas}$.

Kinematic measurements using [C II] do not follow either the ionised gas or molecular gas expectations showing lower σ for higher SFRs at a fixed $M_{\rm gas}$. This is likely due to the the fact that [C II] emission can originate from different phases of the ISM with galaxies having different relative contributions from e.g., photo-dissociated regions, neutral gas, CO-dark molecular gas, and ionised gas. When split in SFR bins, the [C II] sample behaves as expected with the high SFR (low metallicity) having low dispersions at a fixed $M_{\rm gas}$.

To further pick out the physical meaning underlying the scatter of velocity dispersion in disc galaxies, large kinematic surveys with reliable molecular gas tracers, SFR indicators, and kinematics are needed. However, the underlying driver or maintenance mode of turbulence likely acts on much smaller scales requiring a 'PHANGS-like' survey at higher redshift with highly resolved ionised and multiple molecular gas tracers in the *same* galaxies allowing an investigation of $\Sigma_{\rm SFR}$, residual velocities, and winds, well below the kpc-scale. For ionised gas, this will only be feasible with 30m telescopes at $z > 1$ and the new MAVIS IFU at $z < 1$, and for molecular gas with upgraded sub-millimetre facilities.

ACKNOWLEDGEMENTS

EW is grateful for the encouragement and feedback from P. Sharda, K. Glazebrook, S. Brough, M. Kaasinen. EW acknowledges support by the Australian Research Council Centre of Excellence for All Sky Astrophysics in 3 Dimensions (ASTRO 3D), through project number CE170100013. EW acknowledges the support of the Kavli Institute for Cosmology, Cambridge Visitor scheme. HÜ acknowledges funding by the European Union (ERC APEX, 101164796). Views and opinions expressed are however those of the authors only and do not necessarily reflect those of the European Union or the European Research Council Executive Agency. Neither the European Union nor the granting authority can be held responsible for them.

DATA AVAILABILITY

This paper takes advantage of data literature sources as described in Section 2. Parameters have been adjusted from originally published sources to homogenise techniques where feasible. The data compilation for this analysis will be provided online.

REFERENCES

Aditya K., 2023, MNRAS, 522, 2543
Aditya K., 2024, MNRAS, 532, 3839
Adscheid S., et al., 2024, A&A, 685, A1
Alaghband-Zadeh S., et al., 2013, MNRAS, 435, 1493
Bacchini C., et al., 2024, A&A, 687, A115
Barišić I., et al., 2024, arXiv e-prints, p. arXiv:2408.08350
Belokurov V., Kravtsov A., 2022, MNRAS, 514, 689
Binney J., Tremaine S., 2008, Galactic Dynamics: Second Edition. Princeton University Press
Bird J. C., Kazantzidis S., Weinberg D. H., Guedes J., Callegari S., Mayer L., Madau P., 2013, ApJ, 773, 43
Bird J. C., Loebman S. R., Weinberg D. H., Brooks A. M., Quinn T. R., Christensen C. R., 2021, MNRAS, 503, 1815
Boselli A., Gavazzi G., Lequeux J., Pierini D., 2002, A&A, 385, 454
Bothwell M. S., Maiolino R., Peng Y., Cicone C., Griffith H., Wagg J., 2016, MNRAS, 455, 1156
Bouché N., Carfantan H., Schroetter I., Michel-Dansac L., Contini T., 2015, AJ, 150, 92
Bournaud F., Elmegreen B. G., Elmegreen D. M., 2007, ApJ, 670, 237
Burkert A., et al., 2010, ApJ, 725, 2324
Burkert A., et al., 2016, ApJ, 826, 214
Carilli C., Walter F., 2013, preprint, (arXiv:1301.0371)
Chabrier G., 2003, PASP, 115, 763
Clark P. C., Glover S. C. O., Ragan S. E., Duarte-Cabral A., 2019, MNRAS, 486, 4622
Cortzen I., et al., 2020, A&A, 634, L14
Cowie L. L., Hu E. M., Songaila A., 1995, AJ, 110, 1576
Croxall K. V., et al., 2017, ApJ, 845, 96
D'Eugenio F., et al., 2024, Nature Astronomy, 8, 1443
Danhaive A. L., et al., 2025, arXiv e-prints, p. arXiv:2503.21863
Davies R., et al., 2011, ApJ, 741, 69
Davies R., et al., 2018, in Evans C. J., Simard L., Takami H., eds, Society of Photo-Optical Instrumentation Engineers (SPIE) Conference Series Vol. 10702, Ground-based and Airborne Instrumentation for Astronomy VII. p. 1070209 (arXiv:1807.05089), doi:10.1117/12.2311480
Davis T. A., et al., 2013, MNRAS, 429, 534
De Looze I., et al., 2014, A&A, 568, A62
Dessauges-Zavadsky M., et al., 2015, A&A, 577, A50
Dessauges-Zavadsky M., et al., 2020, A&A, 643, A5
Di Teodoro E. M., Fraternali F., 2015, MNRAS, 451, 3021
Di Teodoro E. M., Fraternali F., Miller S. H., 2016, A&A, 594, A77
Dunne L., Maddox S. J., Papadopoulos P. P., Ivison R. J., Gomez H. L., 2022, MNRAS, 517, 962
Eales S., Gomez H., Dunne L., Dye S., Smith M. W. L., 2023, arXiv e-prints, p. arXiv:2303.07376
Ejdetjärn T., Agertz O., Östlin G., Renaud F., Romeo A. B., 2022, MNRAS, 514, 480
Ellis S., et al., 2020, in Evans C. J., Bryant J. J., Motohara K., eds, Society of Photo-Optical Instrumentation Engineers (SPIE) Conference Series Vol. 11447, Ground-based and Airborne Instrumentation for Astronomy VIII. p. 11447A0, doi:10.1117/12.2561930
Elmegreen B. G., Elmegreen D. M., 2006, ApJ, 650, 644
Elmegreen D. M., Elmegreen B. G., Ravindranath S., Coe D. A., 2007, ApJ, 658, 763
Elmegreen B. G., Elmegreen D. M., Tompkins B., Jenks L. G., 2017, ApJ, 847, 14
Faucher-Giguère C.-A., Quataert E., Hopkins P. F., 2013, MNRAS, 433, 1970
Fisher D. B., Bolatto A. D., White H., Glazebrook K., Abraham R. G., Obreschkow D., 2019, ApJ, 870, 46
Font A. S., Navarro J. F., Stadel J., Quinn T., 2001, ApJ, 563, L1
Förster Schreiber N. M., et al., 2006, ApJ, 645, 1062
Förster Schreiber N. M., et al., 2009, ApJ, 706, 1364
Fraternali F., Karim A., Magnelli B., Gómez-Guijarro C., Jiménez-Andrade E. F., Posses A. C., 2021, A&A, 647, A194
Fujimoto S., et al., 2021, ApJ, 911, 99
Fujimoto S., et al., 2024, arXiv e-prints, p. arXiv:2402.18543

Genzel R., et al., 2011, ApJ, 733, 101
Genzel R., et al., 2015, ApJ, 800, 20
Girard M., et al., 2021, ApJ, 909, 12
Glazebrook K., Ellis R., Santiago B., Griffiths R., 1995, MNRAS, 275, L19
Goldsmith P. F., Langer W. D., Pineda J. L., Velusamy T., 2012, ApJS, 203, 13
Green A. W., et al., 2010, Nature, 467, 684
Guo Y., et al., 2014, preprint, (arXiv:1410.7398)
Gurman A., Hu C.-Y., Sternberg A., van Dishoeck E. F., 2024, ApJ, 965, 179
Hamilton-Campos K. A., Simons R. C., Peeples M. S., Snyder G. F., Heckman T. M., 2023, arXiv e-prints, p. arXiv:2303.04171
Herrera-Camus R., et al., 2015, ApJ, 800, 1
Herrera-Camus R., et al., 2022, A&A, 665, L8
Hodge J. A., Carilli C. L., Walter F., de Blok W. J. G., Riechers D., Daddi E., Lentati L., 2012, ApJ, 760, 11
Huertas-Company M., et al., 2023, arXiv e-prints, p. arXiv:2305.02478
Hung C.-L., et al., 2019, MNRAS, 482, 5125
Ikeda M., Oka T., Tatematsu K., Sekimoto Y., Yamamoto S., 2002, ApJS, 139, 467
Immeli A., Samland M., Westera P., Gerhard O., 2004, ApJ, 611, 20
Jacobs C., et al., 2023, ApJ, 948, L13
Jiménez E., Lagos C. d. P., Ludlow A. D., Wisnioski E., 2023, MNRAS, 524, 4346
Johnson H. L., et al., 2018, MNRAS, 474, 5076
Jones G. C., et al., 2016, ApJ, 830, 63
Jones G. C., et al., 2021, MNRAS, 507, 3540
Kaasinen M., et al., 2020, ApJ, 899, 37
Kassin S. A., et al., 2012, ApJ, 758, 106
Kassin S. A., Brooks A., Governato F., Weiner B. J., Gardner J. P., 2014, ApJ, 790, 89
Kim W.-T., Ostriker E. C., Stone J. M., 2002, ApJ, 581, 1080
Kohandel M., Pallottini A., Ferrara A., Zanella A., Rizzo F., Carniani S., 2024, A&A, 685, A72
Kretschmer M., Dekel A., Teyssier R., 2022, MNRAS, 510, 3266
Krumholz M. R., Burkhart B., 2016, MNRAS, 458, 1671
Krumholz M. R., Burkhart B., Forbes J. C., Crocker R. M., 2018, MNRAS, 477, 2716
Kuhn V., Guo Y., Martin A., Bayless J., Gates E., Puleo A., 2024, ApJ, 968, L15
Law D. R., Steidel C. C., Erb D. K., Larkin J. E., Pettini M., Shapley A. E., Wright S. A., 2009, ApJ, 697, 2057
Law D. R., et al., 2022, ApJ, 928, 58
Le Bail A., et al., 2023, arXiv e-prints, p. arXiv:2307.07599
Leaman R., et al., 2017, MNRAS, 472, 1879
Lee L. L., et al., 2024a, arXiv e-prints, p. arXiv:2411.07312
Lee J. H., Park C., Hwang H. S., Kwon M., 2024b, ApJ, 966, 113
Lehnert M. D., Nesvadba N. P. H., Tiran L. L., Di Matteo P., van Driel W., Douglas L. S., Chemin L., Bournaud F., 2009, ApJ, 699, 1660
Leja J., et al., 2022, ApJ, 936, 165
Lelli F., Di Teodoro E. M., Fraternali F., Man A. W. S., Zhang Z.-Y., De Breuck C., Davis T. A., Maiolino R., 2021, Science, 371, 713
Lelli F., et al., 2023, A&A, 672, A106
Lenkić L., et al., 2023, ApJ, 945, 9
Leslie S. K., et al., 2020, ApJ, 899, 58
Lian J., Luo L., 2024, ApJ, 960, L10
Liang L., et al., 2024, MNRAS, 528, 499
Liu D., et al., 2019a, ApJS, 244, 40
Liu D., et al., 2019b, ApJ, 887, 235
Mackereth J. T., et al., 2019, MNRAS, 482, 3426
Madden S. C., et al., 2020, A&A, 643, A141
Mannucci F., Cresci G., Maiolino R., Marconi A., Gnerucci A., 2010, MNRAS, 408, 2115
McCluskey F., Wetzel A., Loebman S. R., Moreno J., Faucher-Giguère C.-A., Hopkins P. F., 2024, MNRAS, 527, 6926
McGaugh S. S., Schombert J. M., Bothun G. D., de Blok W. J. G., 2000, ApJ, 533, L99
Meng X., Gnedin O. Y., Li H., 2019, MNRAS, 486, 1574
Narayanan D., Krumholz M. R., 2017, MNRAS, 467, 50
Neeleman M., Prochaska J. X., Kanekar N., Rafelski M., 2020a, qubefit: MCMC kinematic modeling, Astrophysics Source Code Library, record ascl:2005.013
Neeleman M., Prochaska J. X., Kanekar N., Rafelski M., 2020b, Nature, 581, 269
Nelson E. J., et al., 2023a, arXiv e-prints, p. arXiv:2310.06887
Nelson E. J., et al., 2023b, ApJ, 948, L18
Nipoti C., 2023, MNRAS, 518, 5154
Olsen K. P., Greve T. R., Narayanan D., Thompson R., Toft S., Brinch C., 2015, ApJ, 814, 76
Orr M. E., et al., 2020, MNRAS, 496, 1620
Parlanti E., Carniani S., Pallottini A., Cignoni M., Cresci G., Kohandel M., Mannucci F., Marconi A., 2023, A&A, 673, A153
Parlanti E., et al., 2024, arXiv e-prints, p. arXiv:2407.19008
Pineda J. L., Langer W. D., Goldsmith P. F., 2014, A&A, 570, A121
Popesso P., et al., 2023, MNRAS, 519, 1526
Posses A. C., et al., 2023, A&A, 669, A46
Price S. H., et al., 2016, ApJ, 819, 80
Price S. H., et al., 2021, ApJ, 922, 143
Rathjen T.-E., Naab T., Walch S., Seifried D., Girichidis P., Wünsch R., 2023, MNRAS, 522, 1843
Renaud F., Romeo A. B., Agertz O., 2021, MNRAS, 508, 352
Reshetnikov V. P., Dettmar R.-J., Combes F., 2003, A&A, 399, 879
Rey M. P., et al., 2023, MNRAS, 521, 995
Rizzo F., Vegetti S., Fraternali F., Di Teodoro E., 2018, MNRAS, 481, 5606
Rizzo F., Vegetti S., Powell D., Fraternali F., McKean J. P., Stacey H. R., White S. D. M., 2020, Nature, 584, 201
Rizzo F., Vegetti S., Fraternali F., Stacey H. R., Powell D., 2021, MNRAS, 507, 3952
Rizzo F., Kohandel M., Pallottini A., Zanella A., Ferrara A., Vallini L., Toft S., 2022, A&A, 667, A5
Rizzo F., et al., 2023, A&A, 679, A129
Rizzo F., et al., 2024, A&A, 689, A273
Robertson B. E., et al., 2023, ApJ, 942, L42
Rodrigues M., Hammer F., Flores H., Puech M., Athanassoula E., 2017, MNRAS, 465, 1157
Romeo A. B., Falstad N., 2013, MNRAS, 433, 1389
Romeo A. B., Wiegert J., 2011, MNRAS, 416, 1191
Romeo A. B., Burkert A., Agertz O., 2010, MNRAS, 407, 1223
Rubin R. H., 1985, ApJS, 57, 349
Salim D. M., Federrath C., Kewley L. J., 2015, ApJ, 806, L36
Schaerer D., et al., 2020, A&A, 643, A3
Scoville N., et al., 2017, ApJ, 837, 150
Shao Y., et al., 2022, A&A, 668, A121
Shapiro K. L., et al., 2008, ApJ, 682, 231
Sharma S., Hayden M. R., Bland-Hawthorn J., 2021, MNRAS, 507, 5882
Simons R. C., et al., 2017, ApJ, 843, 46
Simons R. C., et al., 2019, ApJ, 874, 59
Smit R., et al., 2018, Nature, 553, 178
Speagle J. S., Steinhardt C. L., Capak P. L., Silverman J. D., 2014, ApJS, 214, 15
Spitzer Lyman J., Schwarzschild M., 1951, ApJ, 114, 385
Swinbank A. M., et al., 2011, ApJ, 742, 11
Tacconi L. J., et al., 2008, ApJ, 680, 246
Tacconi L. J., et al., 2013, ApJ, 768, 74
Tacconi L. J., et al., 2018, ApJ, 853, 179
Tacconi L. J., Genzel R., Sternberg A., 2020, ARA&A, 58, 157
Tadaki K., et al., 2018, Nature, 560, 613
Tadaki K.-i., et al., 2020a, ApJ, 889, 141
Tadaki K.-i., et al., 2020b, ApJ, 901, 74
Tamfal T., Mayer L., Quinn T. R., Babul A., Madau P., Capelo P. R., Shen S., Staub M., 2022, ApJ, 928, 106
Thorne J. E., et al., 2021, MNRAS, 505, 540
Toomre A., 1964, ApJ, 139, 1217
Tsukui T., Iguchi S., 2021, Science, 372, 1201
Tsukui T., Wisnioski E., Krumholz M. R., Battisti A., 2023, MNRAS, 523, 4654

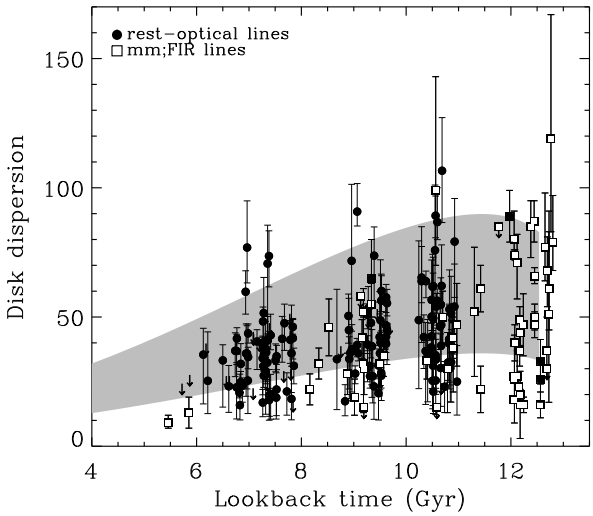

Figure A1. Same as Fig.2 with a linear dispersion axis and a time axis represented in Gyrs.

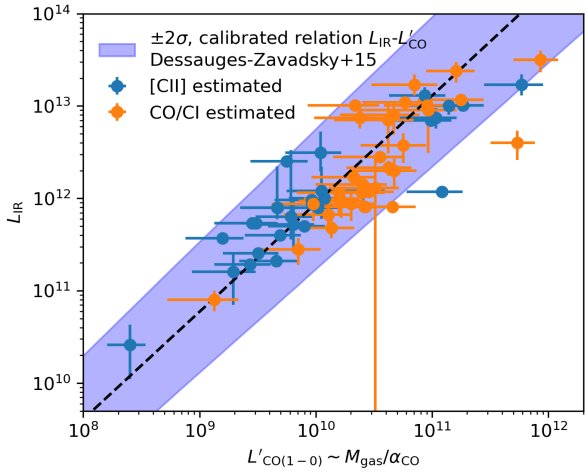

Figure A2. Values of L(IR) as a function of L(CO) for sources with different gas mass tracers discussed in Section 2. The relation calibrated in Dessauges-Zavadsky et al. (2015) is shown by the black dashed line and corresponding 2σ region in purple shading.

Tsukui T., Wisnioski E., Bland-Hawthorn J., Freeman K., 2024, arXiv e-prints, p. arXiv:2409.15909
Tully R. B., Fisher J. R., 1977, A&A, 54, 661
Tully R. B., Fouque P., 1985, ApJS, 58, 67
Übler H., et al., 2017, ApJ, 842, 121
Übler H., et al., 2018, ApJ, 854, L24
Übler H., et al., 2019, ApJ, 880, 48
Übler H., et al., 2024a, MNRAS, 527, 9206
Übler H., et al., 2024b, MNRAS, 533, 4287
Varidel M. R., et al., 2019, MNRAS, 485, 4024
Varidel M. R., et al., 2020, MNRAS, 495, 2265
Vega-Ferrero J., et al., 2023, arXiv e-prints, p. arXiv:2302.07277
Wang B., Silk J., 1994, ApJ, 427, 759
Ward D. B., Dennison B., Gull G., Harwit M., 1975, ApJ, 202, L31
Westfall K. B., Andersen D. R., Bershady M. A., Martinsson T. P. K., Swaters R. A., Verheijen M. A. W., 2014, ApJ, 785, 43
Whitaker K. E., et al., 2014, ApJ, 795, 104
White H. A., et al., 2017, ApJ, 846, 35
Wisnioski E., Glazebrook K., Blake C., Poole G. B., Green A. W., Wyder T., Martin C., 2012, MNRAS, 422, 3339
Wisnioski E., et al., 2015, ApJ, 799, 209
Wisnioski E., et al., 2019, ApJ, 886, 124
Wuyts S., et al., 2011, ApJ, 742, 96
Wuyts S., et al., 2012, ApJ, 753, 114
Zanella A., et al., 2018, MNRAS, 481, 1976
de Graaff A., et al., 2024, A&A, 684, A87
van den Bergh S., Abraham R. G., Ellis R. S., Tanvir N. R., Santiago B. X., Glazebrook K. G., 1996, AJ, 112, 359
van der Wel A., et al., 2014, ApJ, 792, L6

APPENDIX A: DATA COMPILATION

We reproduce Fig. 2 in Fig. A1 to show the evolution as a direct function of lookback time. In Fig. A2 we show the conversion from infrared luminosity, $L_{\rm IR}$, to $M_{\rm gas}$ as described in Section 2.2.

APPENDIX B: ROLE OF MAIN SEQUENCE OFFSET

There are many competing factors when exploring the shape and scatter of $\sigma(z)$. For simpicity, the main text focuses on MS galaxies, however galaxies offset from the MS may not be well represented by the model due to the connection with molecular gas content. Here we reproduce Fig. 5 and Fig. 7 with data points colour-coded by offset from the MS. A clear trend with ΔMS is not obvious from Fig. B1 likely due to the number of variables that can cause scatter in the kinematic measurements. In the lower panels, the outliers with high V/σ are offset above the MS, contrary to expectations from Section 3.1. This may result from the different phases traced by [C II] in different galaxies (Section 4.2.1). In Fig. B2, a reproduction of Fig. 7, the trends seen in the main text hold. Galaxies with high SFRs tend to have large ΔMS values producing a similar rough separation.

This paper has been typeset from a TEX/LATEX file prepared by the author.

Table A1. Compiled kinematic measurementsc*(Full table in published version and online materials)*

Object	Kinematic Paper	RA	DEC	redshift	resolved line	σ [km s^{-1}]	V/σ	Measurement technique[a]
EGS12007881	Tacconi et al. (2013)	14:18:03.60	52:30:22.20	1.160	CO(3 − 2)	$32.0^{+6.0}_{-6.0}$	$7.3^{+2.0}_{-2.0}$	data
EGS13003805	Tacconi et al. (2013)	14:19:40.10	52:49:39.10	1.230	CO(3 − 2)	$46.0^{+11.0}_{-11.0}$	$7.8^{+2.2}_{-2.2}$	data
EGS13011166	Tacconi et al. (2013)	14:19:45.00	52:52:28.00	1.530	CO(3 − 2)	$55.0^{8.0}_{-8.0}$	$6.7^{+1.5}_{-1.5}$	data
EGS4-24985	Übler et al. (2018)	04:19:26.66	52:51:17.00	1.400	CO(3 − 2)	$19.0^{+7.0}_{-7.0}$	$15.6^{+0.4}_{-0.4}$	DYSMAL
BRI1335-0417	Tsukui & Iguchi (2021)	13:38:03.42	-04:32:35.02	4.407	[C II]	$71.0^{+14.0}_{-11.0}$	$2.5^{+0.6}_{-0.4}$	data
zC400569	Lelli et al. (2023)	...	...	2.240	CO(4 − 3)	< 15.0	> 16.0	3D BAROLO
zC488879	Lelli et al. (2023)	...	...	1.470	CO(3 − 2)	< 15.0	> 22.4	3D BAROLO

[a] Technique used to measure kinematic parameters: data = data driven techniques including using the outer regions; DysmalPy (Price et al. 2021); GALPAK3D (Bouché et al. 2015); QubeFit (Neeleman et al. 2020a); 3D BAROLO (Di Teodoro & Fraternali 2015)

Table A2. Compiled galaxy properties *(Full table in published version and online materials)*

Object	$\log(M_*/\mathrm{M}_\odot])$	Source	$\log(M_{\mathrm{gas}}/\mathrm{M}_\odot])$	M_{gas} tracer	Source	SFR [$\mathrm{M}_\odot$ yr^{-1}]	Source
EGS12007881	10.72	Tacconi et al. (2013)	10.86	CO(3 − 2)	Tacconi et al. (2013)	94.0	Tacconi et al. (2013)
EGS13003805	11.23	Tacconi et al. (2013)	11.31	CO(3 − 2)	Tacconi et al. (2013)	200.0	Tacconi et al. (2013)
EGS13011166	11.08	Tacconi et al. (2013)	11.39	CO(3 − 2)	Tacconi et al. (2013)	373.0	Tacconi et al. (2013)
EGS4-24985	10.87	Übler et al. (2018)	10.84	CO(3 − 2)	Übler et al. (2018)	98.8	Übler et al. (2018)
BRI1335-0417	...	...	10.75	CO(2 − 1)	Jones et al. (2016)	1700.0	Tsukui et al. (2023)
zC400569	11.30	Liu et al. (2019a)	11.07	CO(3 − 2)	Lelli et al. (2023)	81.0	Liu et al. (2019a)
zC488879	11.79	Liu et al. (2019a)	10.84	CO(2 − 1)	Lelli et al. (2023)	115.0	Liu et al. (2019a)

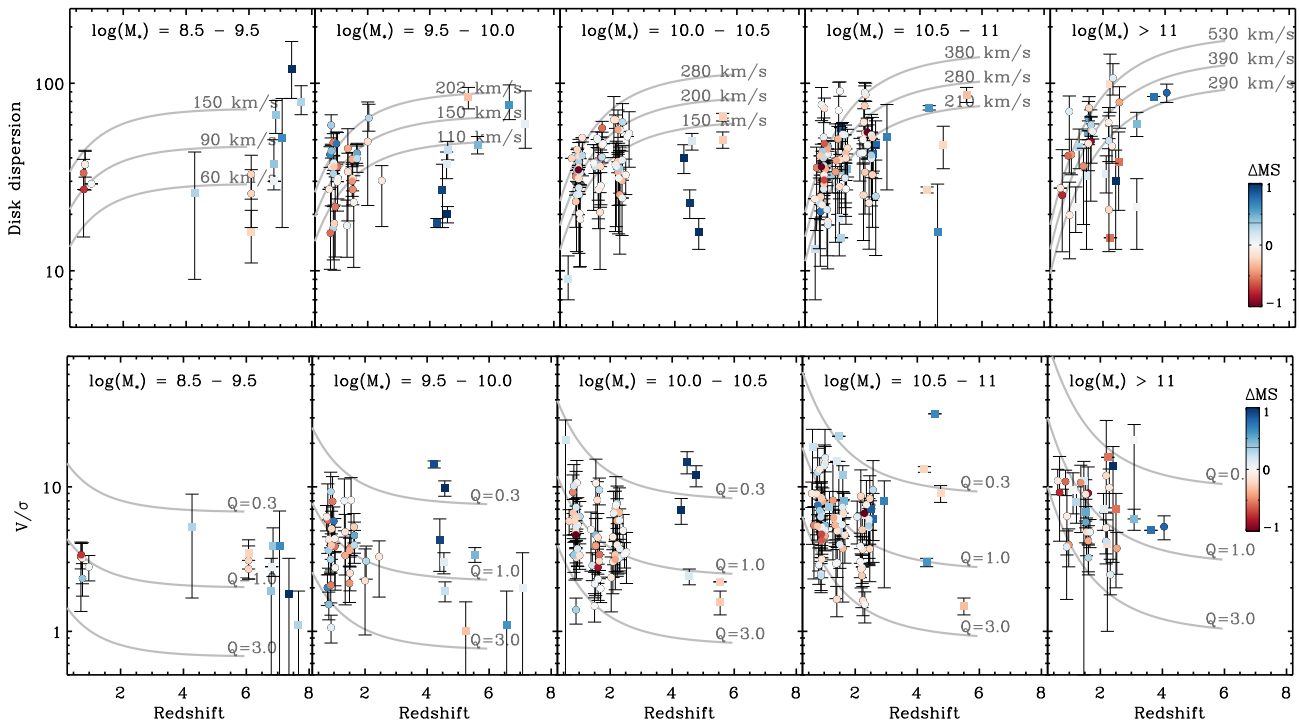

Figure B1. Same as Fig.5 with data points colour-coded by ΔMS.

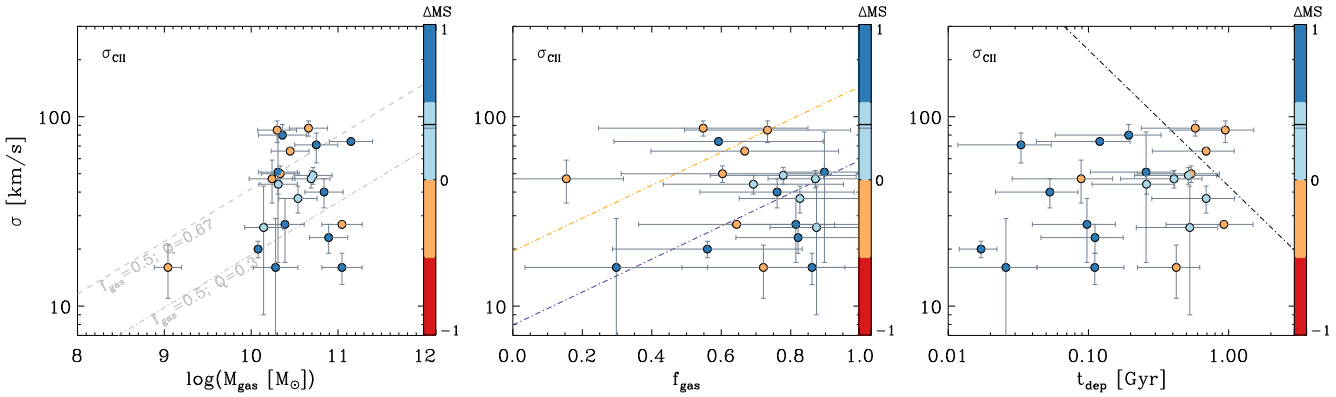

Figure B2. Same as Fig.7 with data points colour-coded by ΔMS.